A General Circulation Model Study of the Atmospheric Response to Extratropical SST Anomalies Observed in 1950–79

NGAR-CHEUNG LAU AND MARY JO NATH

Geophysical Fluid Dynamics Laboratory/NOAA, Princeton University, Princeton, New Jersey

(Manuscript received 20 February 1989, in final form 28 August 1989)

ABSTRACT

A 30-year experiment with an atmospheric general circulation model has been performed. The lower boundary condition at all oceanic grid points between 38°S and 60°N has been prescribed to follow the observed month-to-month variation of the sea surface temperature (SST) field during the 1950–79 period. Much of the model diagnosis presented here pertains to the midlatitude atmospheric response to recurrent SST patterns in the North Pacific and North Atlantic in winter.

The principal modes of variability of the seasonally averaged 515 mb height and SST fields have been identified using rotated principal component (RPC) analysis. The extrema of the first atmospheric mode reside over the North Atlantic and Eurasia, whereas the second mode is associated with height anomalies in the North Pacific/North American sector. Cross-correlation analysis reveals that these two atmospheric modes are linked to leading patterns of the SST field in the North Atlantic and North Pacific, respectively. It is also demonstrated that the extrema in leading RPC patterns of the SST field in the northern oceans are almost coincident with the sites of maximal covariability between the SST and 515 mb height fields.

Regression charts of selected model parameters versus the SST variations off the Newfoundland coast and northwest of Hawaii have been constructed. These two reference maritime sites have been identified by the RPC and cross-correlation analyses as being correlated with the strongest atmospheric signals. The model fields examined in this manner include the geopotential height at various pressure levels, precipitation, heat flux across the air–sea interface, as well as temporal variance and covariance statistics. These regression maps indicate that the atmospheric response to midlatitude SST anomalies has an equivalent barotropic structure. The presence of SST perturbations in the extratropics are associated with displacements of the storm track axes, and with relocations of the midlatitude rainbelts and preferred sites of heat transfer from the underlying ocean. The changes in the locality of synoptic scale eddy activity are accompanied by alterations in the transient eddy forcing of the quasi-stationary flow. The geopotential height tendencies associated with these anomalous eddy effects exhibit a positive spatial correlation with the seasonally averaged, downstream atmospheric response. The time scale for the eddy induced tendencies to produce such seasonal height anomalies is on the order of several days. These findings suggest that the transient disturbances act as an essential intermediary between the extratropical SST forcing and the time-mean atmospheric response.

The principal atmospheric anomaly pattern in the North Atlantic/Eurasian sector exhibits substantial correlations with SST fluctuations in the tropical South Atlantic; whereas oceanic anomalies in the equatorial Pacific are only weakly associated with atmospheric circulation changes in the North Pacific/North American region.

The temporal lead/lag relationships between the simulated atmospheric anomalies and the prescribed SST changes have been explored.

1. Introduction

The extent to which the observed low frequency atmospheric variability may be attributed to fluctuations in the surface properties of the World Oceans has long been a subject of interest to investigators of large-scale dynamical processes as well as long-range weather forecasters. Partially as a result of the intense research efforts devoted to the El Niño–Southern Oscillation phenomena, much attention has recently been focused on the response of the atmospheric circulation to anomalous sea surface temperature (SST) episodes occurring in the near-equatorial oceans. There now exists a considerable amount of observational evidence linking SST variability in the tropics to changes in the midlatitude flow pattern, especially in the Northern Hemisphere during winter (e.g., see Bjerknes 1966 and 1969; Horel and Wallace 1981; van Loon and Rogers 1981; Chen 1982). These empirical results have motivated a wide variety of modeling and theoretical studies aimed at understanding the nature of the extratropical response to remote forcing mechanisms situated in the tropical zone. Among such investigations are simulation experiments using comprehensive general circulation models (GCMs) with prescribed tropical SST

Corresponding author address: Dr. Ngar-Cheung Lau, NOAA, Geophysical Fluid Dynamics Laboratory, Princeton University, P.O. Box 308, Princeton, New Jersey 08542.

anomalies (e.g., Rowntree 1972 and 1976; Keshavamurty 1982; Blackmon et al. 1983; Shukla and Wallace 1983; Palmer and Mansfield 1984; Boer 1985; Lau 1985; von Storch and Kruse 1985; Tokioka et al. 1986), as well as analyses of more idealized mechanistic models (e.g., Hoskins and Karoly 1981; Simmons 1982).

In comparison to the voluminous works on the role of tropical oceans in atmospheric variability, much less emphasis has been given during the past decade to the impacts of midlatitude SST anomalies on the circulation patterns. The in situ interaction between the ocean and the atmosphere in the extratropics is by no means an unexplored issue. Extended range forecasters have long recognized the importance of extratropical SST variations in the North Atlantic and North Pacific as predictors of the climate over North America and Europe on monthly and seasonal time scales (e.g., see Namias 1969; Namias and Cayan 1981; Namias et al. 1988; Ratcliffe and Murray 1970). More recently, the myriad physical and dynamical processes relevant to air–sea feedback in the middle latitudes have been described in a comprehensive review by Frankignoul (1985). Palmer and Sun (1985) have presented new observational evidence on the relationship between SST fluctuations off the Newfoundland coast and various wintertime meteorological anomalies in the North Atlantic/European sector. The nature of the observed air–sea interaction in the extratropics has also been examined in a systematic study by Wallace and Jiang (1987, hereafter referred to as WJ). The latter work emphasized the atmospheric signals associated with SST changes at two maritime sites in the middle latitudes. The North Atlantic site selected in their study is also located in the vicinity of the Newfoundland coast. The polarity of SST fluctuations at this site tends to be opposite to that in the Bermuda region. This north–south oriented dipole in the SST field is shown to be strongly correlated with the western-Atlantic (WA) teleconnection pattern in the 500 mb height field. The second oceanic site investigated by WJ lies to the northwest of the Hawaiian Islands, where the SST varies in opposition to that along the west coast of North America. This east–west seesaw in the SST field is seen to exhibit a distinct relationship with the atmospheric Pacific/North American (PNA) pattern. Similar associations between the PNA pattern and the east–west SST seesaw in the North Pacific have previously been noted by Lanzante (1984). Both the WA and PNA patterns have been identified by Wallace and Gutzler (1981) as prominent modes of low frequency variability of the flow field in the middle and upper troposphere during winter. These teleconnection patterns depict standing oscillations of the geopotential height field with a well defined set of geographically fixed nodes and antinodes. WJ further noted that the response of such teleconnection patterns to the extratropical SST changes appears to be even stronger than the atmospheric signals associated with El Niño events in the tropical Pacific. These empirical studies hence imply that the role of SST fluctuations in the extratropics cannot be neglected in any comprehensive treatment of the variability of the atmosphere-ocean climate system.

Further diagnosis of the observational SST and atmospheric records, as reported by Wallace et al. (1990, hereafter referred to as WSJ) in the same issue of this journal, has provided evidence on the strong simultaneous relationships between the principal atmospheric teleconnection patterns and leading eigenvectors of the extratropical SST field. These authors have also noted interesting correlations between leading eigenvectors of the SST *tendency* and characteristic atmospheric patterns over the extratropical western Pacific and western Atlantic. The latter finding suggests that a considerable portion of the SST variability in the extratropical western oceans may be a manifestation of the oceanic response to local atmospheric forcing.

Observational results on the importance of midlatitude SST perturbations have stimulated several investigators to launch GCM experiments with prescribed anomalous oceanic forcing in the extratropics. Palmer and Sun (1985) have performed sensitivity experiments with the U.K. Meteorological Office model by imposing idealized warm and cold SST anomalies in the Newfoundland region. They detected a significant atmospheric response downstream of the forcing region, with warm SSTs being accompanied by positive height perturbations over the central North Atlantic, and negative height changes over eastern Europe. They also noted some influence of the SST pattern on the location of the preferred trajectory of synoptic scale disturbances over the Atlantic. The impact of the dipole-like SST anomaly pattern over the North Pacific on the atmospheric flow pattern has been examined by Kutzbach et al. (1977), Shukla and Bangaru (1979), Pitcher et al. (1988) and Frankignoul and Molin (1988). The extensive model runs analyzed by Pitcher et al. are indicative of a PNA-like response to cold anomalies near the dateline and warm anomalies along the North American west coast. However, they reported that the atmospheric response to a SST anomaly pattern with the opposite polarity (i.e., warm waters near the dateline and cold waters in the eastern North Pacific) bears little resemblance to the PNA teleconnection pattern. Thus far, much of the modeling effort is devoted to reproducing the *stationary* response to *temporally* and *spatially fixed* SST anomalies. In many cases, the spatial pattern of the prescribed anomaly is somewhat idealized. Moreover, it is often necessary to impose anomaly amplitudes which are much higher than the observed values, so as to yield statistically significant atmospheric signals. Many scientific issues pertaining to the nature of extratropical air–sea interaction in these model simulations remain to be resolved. Among such outstanding problems are

- the nature of dynamical and physical mechanisms responsible for linking the oceanic forcing to the atmospheric circulation,
- the objective identification of the maritime sites which are most effective in modifying the flow patterns in both the observed and modeled atmospheres, and
- the seasonal dependence of the atmospheric response.

Within the past few years, several long term GCM experiments aimed at understanding the atmospheric effects of tropical Pacific SST anomalies have been conducted at the Geophysical Fluid Dynamics Laboratory (GFDL). Throughout these integrations, the lower boundary conditions at all grid points in the Pacific Basin between 30°S and 30°N latitudes have been prescribed to follow the observed month-to-month SST changes during the 1962–76 period, in which four El Niños of varying intensities occurred. Results of these model runs have been reported by Lau (1985), Lau and Oort (1985), Kang and Lau (1986) and Held and Kang (1987). The experimental design of these integrations allows for the incorporation of the full spatial and temporal variability of realistic oceanic conditions in the forcing domain of interest. The model output may also be utilized to address such issues as the sensitivity of the atmospheric circulation to various locations of the SST forcing, as well as to the timing of the prescribed SST changes with respect to the seasonal cycle. In view of the ample observational evidence on the atmospheric impact of SST anomalies in both the tropical and extratropical portions of the Pacific and the Atlantic, and keeping in mind the advantages to be gained by inserting temporally and spatially varying SST conditions, a new series of GCM runs have recently been performed at GFDL by adopting an experimental design similar to that described above, and by extending the forcing domain to all oceanic grid points lying between 38°S and 60°N (see Fig. 1). The primary objectives of the present paper are to document the model response to SST anomalies located in the North Atlantic and North Pacific during the northern winter, and to investigate the essential dynamical processes involved in air–sea interaction in the extratropics. The model results are to be compared with existing observations cited in the recent literature, especially those reported by WJ and WSJ. Other aspects of this experiment, such as the influences of SSTs in the tropical zone, and the seasonality of the atmospheric response to oceanic forcing, will only be described briefly here.

In this paper, the prominent modes of variability of the model-simulated midtropospheric height field, as well as that of the observed SST input in the North Atlantic and North Pacific, are first determined using rotated principal component analysis. Interrelationships among such recurrent patterns in the geopotential height and SST fields are then sought by cross-correlation analysis (see sections 3 and 4). The most effective maritime sites for altering atmospheric behavior are ascertained by locating the SST sites which account for a substantial fraction of the spatially integrated midtropospheric height variance (section 5). The amplitude and spatial pattern of various model fields accompanying SST changes at the positions thus identified are then documented using regression maps in sections 6 and 7. The role of the transient eddies in linking the midlatitude SST forcing to the seasonally averaged atmospheric signal is examined in section 8. The magnitude of the incremental variability of the model atmosphere attributable to the prescribed SST anomalies is then examined by comparison with the output from a control experiment with no SST fluctuations (section 9). The impact of tropical SST anomalies on the simulated atmospheric circulation is summarized in section 10. The concluding section contains a summary of the essential findings, as well as a discussion on the nature of asynchronous relationships between the model data and the imposed SST anomalies.

2. Description of the experiment

The GCM used for this study has been developed and maintained by the Climate Dynamics Project at GFDL, and is essentially the same as that examined by Manabe and Hahn (1981), Lau (1981), and Lau (1985) in previous atmospheric variability studies. The model had a global domain. Realistic orography and land-sea contrast were incorporated in the lower boundary condition. Horizontal variations of atmospheric fields were expressed in terms of spherical harmonics with a rhomboidal truncation at 15 wavenumbers. Vertical variations were represented at nine discrete sigma levels. The processes in the model physics package included moist convective adjustment, ground hydrology, radiative transfer, formation of sea ice and continental snow cover, and ice-albedo feedback. In the radiative transfer computations, the amount of cloud cover was prescribed as a function of latitude and height only. The seasonal cycle was incorporated by requiring the incoming solar radiation to follow the observed annual march.

In the 30-year duration of the present experiment, the surface temperature at all land points in the model grid was computed by assuming zero heat storage in the ground. On the other hand, the surface temperature at every ocean point between 38°S and 60°N (i.e., the stippled region in Fig. 1) was constrained to follow the month-to-month changes observed locally from January 1950 to December 1979. The SST input for a particular month in the above domain was given by the sum of an invariant climatology and the observed anomaly field for that month. In conformity with the majority of GCM experiments conducted at GFDL during the recent years, the SST climatology for the

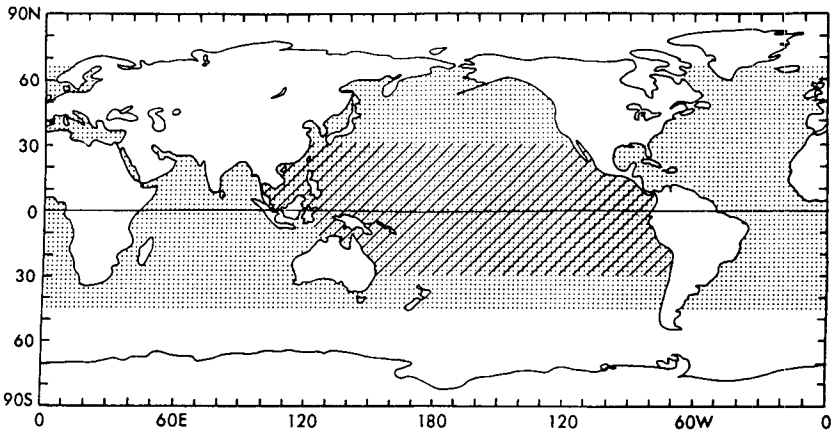

FIG. 1. Stippling indicates those regions in the World Oceans where the observed month-to-month SST variations were prescribed in the present 30-year experiment. Hatching indicates the tropical Pacific region where observed intermonthly changes of the lower boundary condition were imposed in the model runs examined in Lau (1985).

12 calendar months, as compiled by Reynolds (1983) for the 40°S–60°N zone and by Alexander and Mobley (1976) for the high-latitude oceans, was used for the present integration. The individual monthly SST anomalies for the 360-month period was obtained from the objective global analyses of the Comprehensive Ocean Atmosphere Data Set (COADS; see Woodruff et al. 1987). These gridded data were produced by the Observational Studies Project at GFDL, and have a resolution of 1° in the zonal and meridional directions. This data set was interpolated to the Gaussian grid of the spectral model, which has a resolution of approximately 4.5° (latitude) by 7.5° (longitude). The SST condition within the forcing domain was updated every day during the 30-year model run. The daily input was obtained by linear interpolation of the observed monthly mean SST time series, with the assumption that the temperature at the midpoint of each month is equal to the averaged value for that month. Climatological values were assigned to the SSTs over the Arctic and south of approximately 51°S, for which no reliable routine measurements exist. Hence no interannual variability in the SST field has been imposed on those grid points lying in the high latitude oceans. A linear taper was applied to the SST anomalies located at the northern and southern margins of the forcing domain, so that the amplitudes of such anomalies decrease uniformly from the observed values at 38°S (60°N) to zero values at 51°S (68°N).

The integration was initiated using a set of atmospheric conditions selected randomly from another experiment based on the same model. Before the actual 30-year experiment was launched, the model atmosphere has been adjusted to the initial SST condition imposed on 1 January 1950 by integrating the GCM with this particular boundary forcing for several months.

In addition to the 30-year model run described above, a control experiment with a duration of ten years has been performed using the same GCM. In the course of the latter integration, no SST anomalies have been prescribed anywhere on the globe, so that the conditions throughout the World Oceans evolved through ten identical annual cycles. Much of the present study is devoted to the diagnosis of the 30-year SST anomaly experiment. The output of the control run is only used in section 9 to assess the incremental model variability attributable to the presence of SST fluctuations.

3. Relating recurrent patterns in the model atmosphere to SST anomalies

In this section, we shall first examine the principal modes of variability in the model atmosphere, and then determine the extent to which such modes are correlated with the SST forcing prescribed at various maritime sites. The prominent atmospheric circulation patterns in the 30-year experiment have been identified by applying a rotated principal component (RPC) analysis to the Northern Hemisphere extratropical 515 mb height field averaged over the three winter months (December, January, and February). Horel (1981) has presented a concise description of this analysis technique. A comprehensive treatment of the RPC methodology has also been given by Richman (1986). In order to enhance the wave-like features of the height field, the zonally averaged values for each winter have been subtracted from the model data for the same winter prior to the analysis. A similar operation has been performed in computing the correlation charts to be presented in Figs. 5, 6, 7, 8 and 17a. The spatial domain being investigated here extends from 20° to 74°N. Horizontal variations within this domain are repre-

sented at 132 model grid points chosen on the basis of equal area considerations. The anomalies at individual grid points have been normalized by the local standard deviations, so that eigenvectors of the correlation (as opposed to covariance) matrix of the height fluctuations were used in the RPC analysis. The stability of the RPCs to variations in the number of eigenvectors included in the rotation procedure has been tested extensively. It was found that rotations of the first 10, 15, 20 and 25 eigenvectors yielded basically the same set of leading RPC patterns. We shall henceforth present the results based on rotation of the first 20 eigenvectors using the varimax method.

In Fig. 2 the distributions of the correlation coefficients between the height anomalies at individual grid points and the temporal coefficients of the (a) first and (b) second RPCs are illustrated. These two leading RPCs of the simulated atmosphere, to be denoted as ATM1 and ATM2, explain 12.5% and 11.0% of the hemispherically integrated variance, respectively. Both the ATM1 and ATM2 patterns are characterized by dipole-like structures over the Atlantic and Pacific Basins, respectively, with wave-like extensions to the continental areas farther downstream. The spatial appearance of these simulated patterns are similar to those of the recurrent anomalies observed in the Atlantic/Eurasian and Pacific/North American sectors [e.g., see (Wallace and Gutzler 1981, Figs. 12 and 16), (Esbensen 1984, Figs. 7 and 12), (Barnston and Livezey 1987, Figs. 9 and 3)]. A set of leading RPCs has also been obtained on the basis of 515 mb height data with the zonal means retained. The ATM1 and ATM2 patterns shown in Fig. 2 appear as the second- and fifth-ranked RPC in the latter computation, and explain 10.8% and 6.9% of the total variance, respectively. The top ranked RPC pattern for the height field with the zonal averaged included (not shown) exhibits a notable degree of zonal symmetry. Since the present study is primarily concerned with the behavior of the longitudinally varying circulation, we shall confine our attention to the atmospheric variability associated with the ATM1 and ATM2 patterns.

The relationships between the ATM1 and ATM2 patterns in the model atmosphere and the varying SST forcing imposed at the lower boundary are illustrated in Fig. 3, which shows the distributions of the correlation coefficients between SST fluctuations at individual grid points and the temporal coefficients for (a) ATM1 and (b) ATM2. Inspection of the global patterns of these correlation values reveals that the most prominent SST signals accompanying ATM1 are located in the Atlantic Basin, whereas ATM2 is mostly associated with SST changes in the Pacific. Hence only the correlation values for the tropical and North Atlantic are plotted in Fig. 3a, and only Pacific data are displayed in Fig. 3b. As a measure of the statistical significance of the correlation coefficients shown in this figure, we note here that the threshold correlation values, as estimated by the two-tailed Student's t-test for 29 independent winter seasons, are 0.31, 0.37 and 0.47 at the 90%, 95% and 99% levels, respectively. The distribution in Fig. 3a indicates that ATM1 is correlated with an Atlantic SST pattern which is characterized by zonally elongated bands with alternating polarities. In the North Atlantic, ATM1 exhibits the strongest correlations with SST fluctuations located in the Labrador Sea, off the coasts of Newfoundland and Nova Scotia, and in the vicinity of the Bahamas. This pattern bears some resemblance to the observed north–south SST seesaw in the extratropical western Atlantic, as noted by WJ (Fig. 5) and WSJ (Fig. 3). Additional extrema at 10°N and 15°S are also evident in Fig. 3a. The SST pattern accompanying ATM2 (Fig. 3b) is dominated by an east–west oriented dipole in the North Pacific, with one center located north of the Hawaiian Islands, and the other center situated west of Baja California. This configuration is similar to the east–west seesaw in the SST anomalies observed in this region (see WJ, Fig. 4; and WSJ, Fig. 1). The absence of any coherent tropical features in Fig. 3b suggests that ATM2 does not bear any strong association with El Niño episodes occurring near the equatorial Pacific in the course of this experiment. We shall return to address the issue of model response to SST anomalies located in the tropical Pacific and Atlantic in section 10.

4. Relating recurrent patterns in the SST forcing to the model response

The apparent relationships between RPC patterns of the model atmosphere and large-scale SST anomaly patterns, as demonstrated in the previous section, are further examined here by taking the complementary approach; i.e., we shall first identify the principal modes of SST variability in the two ocean basins using RPC analysis, and then delineate the correlation between such modal structures in the SST field and the 515 mb height fluctuations at individual grid points. An analogous approach has been adopted by WSJ in delineating simultaneous relationships between the observed SST and atmospheric pressure fields. The correlation patterns in Fig. 3 indicate that, with the exception of the Atlantic extremum at 15°S, a majority of the SST anomaly centers associated with ATM1 and ATM2 are located in the extratropics. We shall henceforth devote our attention to characteristic SST patterns in the North Atlantic and North Pacific. The SST data for each ocean basin have been subjected to a RPC analysis similar to that described in section 3. The domains of analysis extend from 20°N to 56°N, and consist of 39 and 65 points for the North Atlantic and North Pacific, respectively. These maritime points lie on a staggered grid with a resolution of 15° and 4.5° in the zonal and meridional directions, respectively. In view of the considerable degree of "redness" in the SST records for certain sites (e.g., see WSJ, Fig. 2), the SST time series

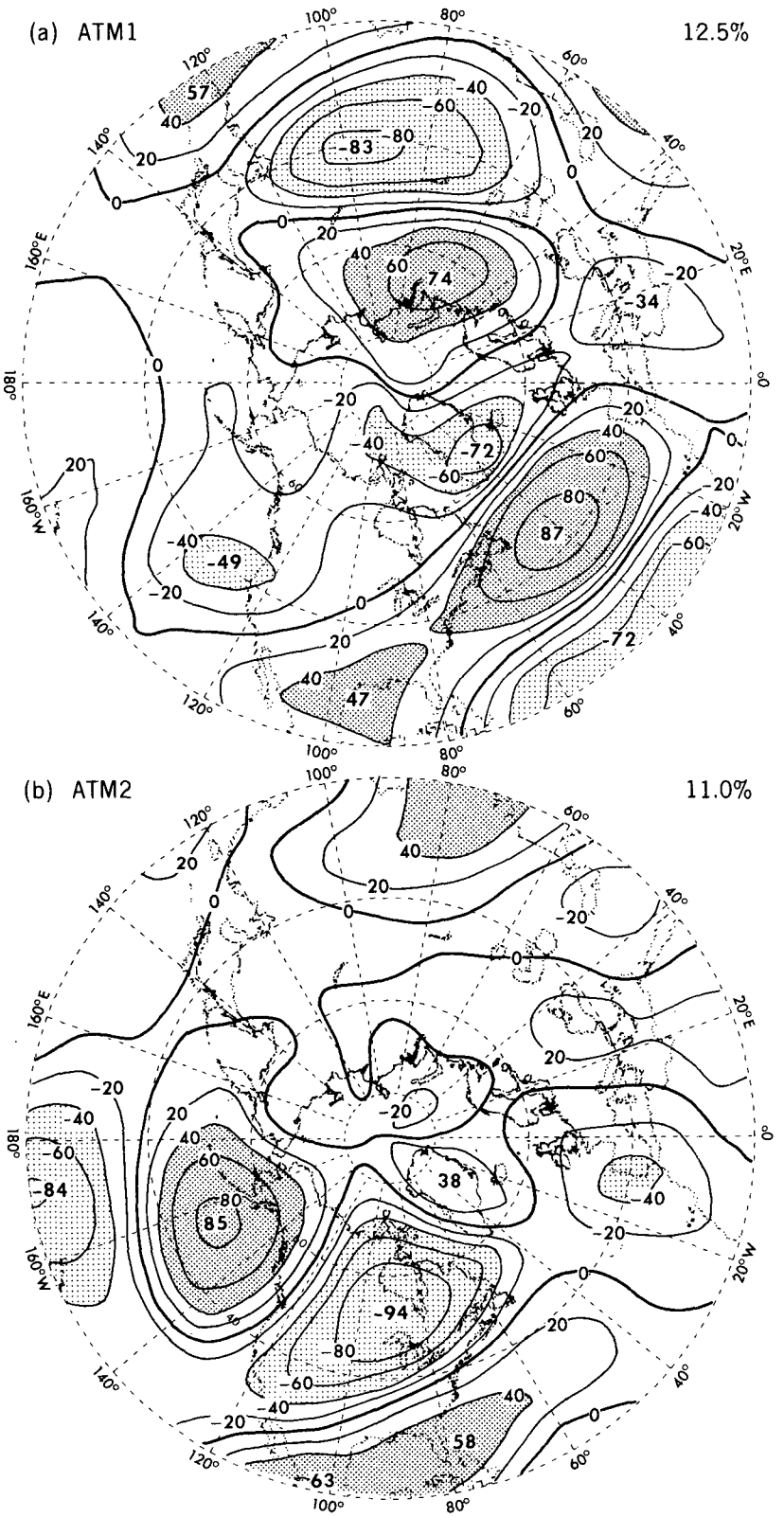

FIG. 2. Distributions of the correlation coefficients (in percent) between 515 mb geopotential height at individual grid points and the temporal coefficients for the (a) first and (b) second RPCs of the 515 mb height field. Contour interval 20%. Heavy and light stippling indicate

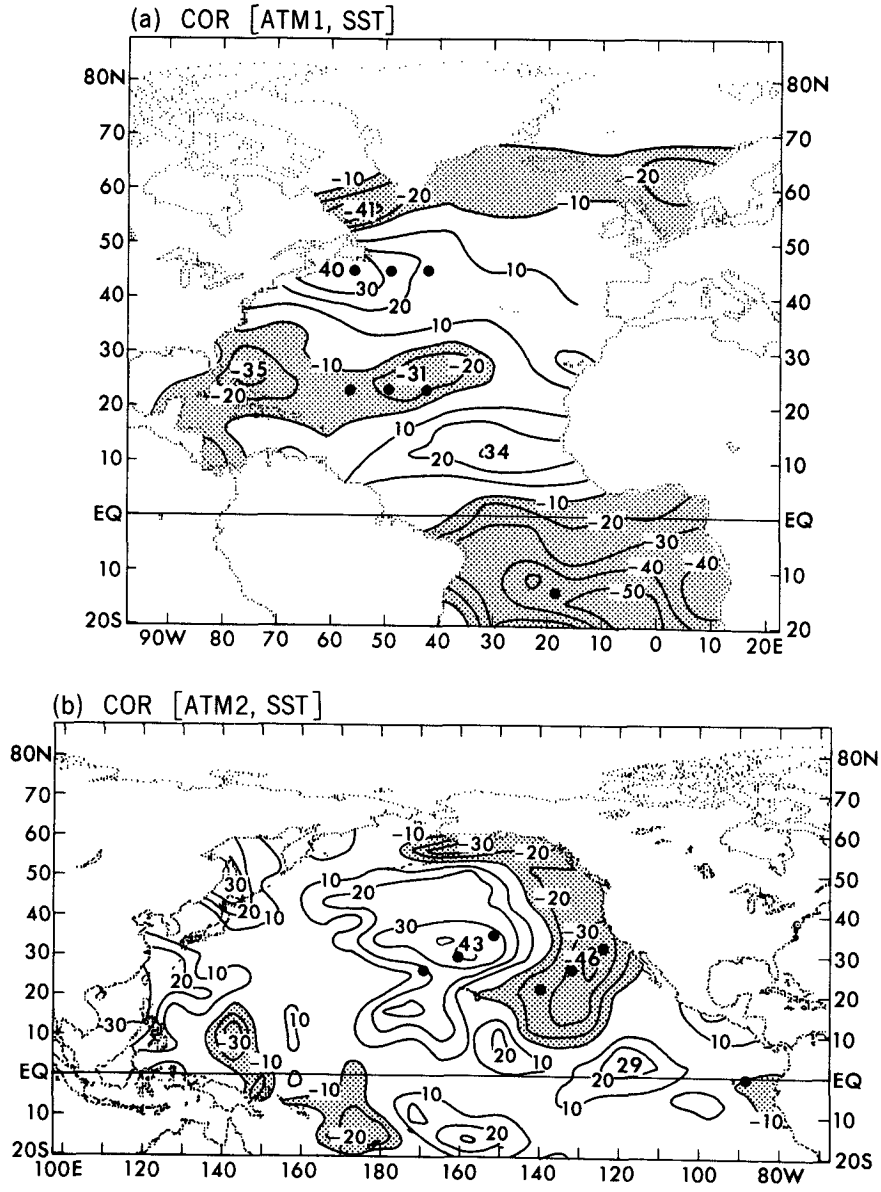

FIG. 3. Distributions of the correlation coefficients (in percent) between SST at individual grid points and the temporal coefficients for the (a) first and (b) second RPCs of the 515 mb height field (see Fig. 2). Contour interval −10%. The zero contour has been omitted. Stippling indicates correlation values less than 10%. The solid dots indicate locations of the centroids of reference SST sites selected for constructing teleconnection charts in the latter part of this study.

at individual grid points have been processed through a bandpass filter. This simple filtering procedure entails the subtraction of 13-month running means from 3-month running means, and serves to remove those signals with temporal scales shorter than a season and much longer than a year. The RPC analysis was then

correlation values larger than 40% and less than −40%, respectively. The fraction of hemispherically integrated variance explained by each mode is indicated at the upper right corner of the corresponding panel. The computations were based on averages of the model data for the three winter months of December, January, and February. The zonally averaged values for individual winter seasons have been removed from the grid point data prior to the analysis. For all charts shown in this paper using the polar stereographic projection, the outermost circle corresponds to the 20°N latitude.

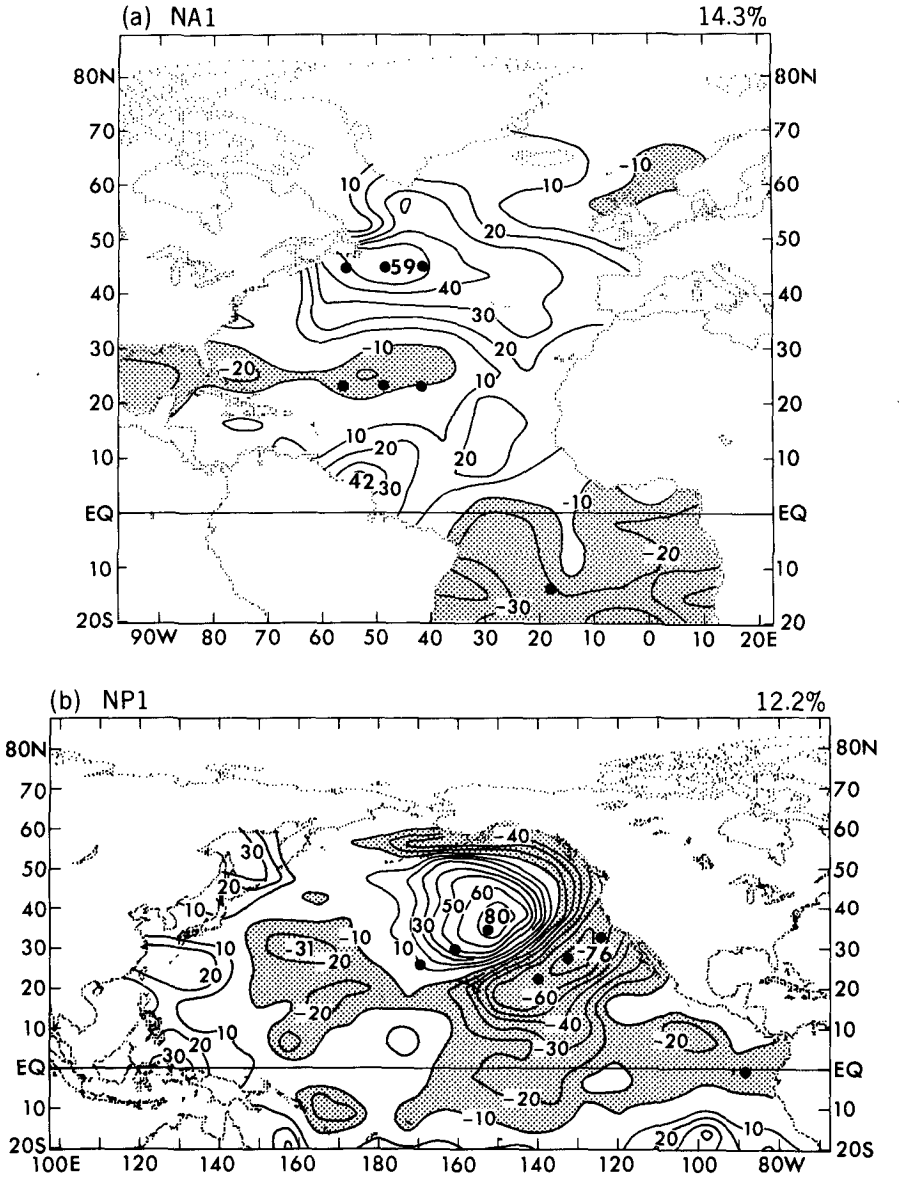

FIG. 4. Distributions of the correlation coefficients (in percent) between SST at individual grid points and the temporal coefficients for the first RPCs of the SST field for the extratropical (a) North Atlantic and (b) North Pacific. Contour interval 10%. The zero contour has been omitted. Stippling indicates correlation values less than −10%. The fraction of spatially integrated variance explained by each mode is indicated at the upper right corner of the corresponding panel. The SST data subjected to the RPC analysis have been processed through a bandpass filter discussed in the text. The computations were based on three-month averages for the northern winter season. The solid dots indicate the locations of the reference SST sites selected for constructing teleconnection charts in the latter part of this study.

conducted separately for each ocean basin using seasonally averaged SST anomalies for 29 winters. We stress here that the bandpass filter described above was used solely in the present RPC analysis of the SST field. All other results in this paper pertaining to the SST field were based on unfiltered data. As in section 3, the rotation was performed on the first 20 eigenvectors. Experimentation with rotations of the first 10, 15, and 25 eigenvectors of the SST fields resulted in similar RPC patterns.

In Fig. 4 are shown the patterns of the correlation coefficients between the SST fluctuations at individual grid points and the temporal coefficients for the leading RPC of the SST field in the (a) North Atlantic and (b) North Pacific. Although the actual RPC analysis has been performed on SST changes occurring north of

20°N, the plotting domain in Fig. 4 was expanded farther southward to 20°S, so as to illustrate the degree of correlation between the extratropical SST modes and the anomalies in the equatorial oceans. The leading RPC patterns for the North Atlantic and North Pacific, hereafter referred to as NA1 and NP1, explain 14.3% and 12.2% of the corresponding domain-integrated variance, respectively.

The spatial pattern of NA1 (Fig. 4a) is comprised of several zonally elongated bands with alternating polarities. The most prominent feature is the zonal belt extending across the North Atlantic at about 45°N, with a local maximum situated southeast of Newfoundland. Other belts with an east–west orientation are discernible at the 25°N, 10°N, and 15°S latitudes. Some of these characteristics are in agreement with those deduced from previous empirical orthogonal function (EOF) analyses of the entire Atlantic Basin (Weare 1977, Fig. 7), the tropical Atlantic (Lough 1986, Fig. 4), and the North Atlantic (WSJ, Fig. 3), as well as from one-point teleconnection charts depicting the north–south SST seesaw in the western North Atlantic (WJ, Fig. 5). There also exist many similarities between NA1 (Fig. 4a) and the SST pattern associated with the ATM1 mode of the 515 mb height field (Fig. 3a), thus implying that ATM1 is correlated with the most recurrent SST pattern in the Atlantic. The latter inference is further substantiated by the evidence presented in Fig. 5a, which shows the distribution of the correlation coefficients between the seasonally averaged 515 mb height at individual grid points with the temporal coefficients for NA1. The notable similarities between Fig. 5a and the spatial pattern of ATM1 (Fig. 2a) confirm that ATM1 and NA1 indeed exhibit a close relationship with each other.

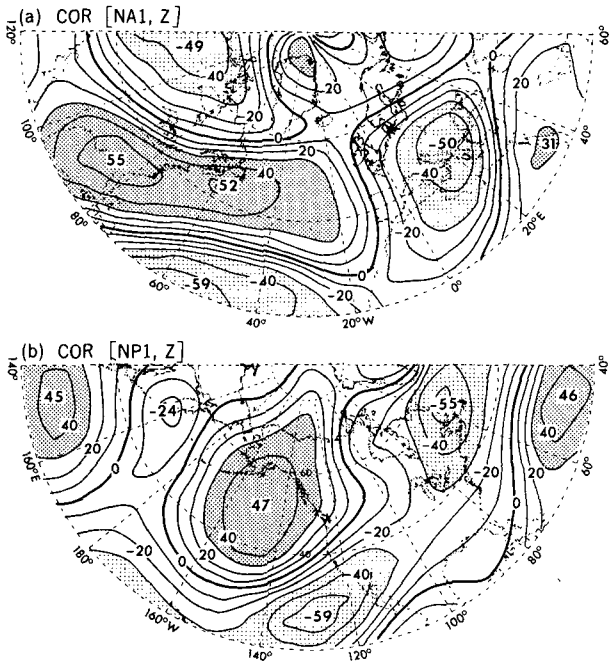

FIG. 5. Distributions of the correlation coefficients (in percent) between 515 mb geopotential height at individual grid points and the temporal coefficients for the first RPCs of the SST field for the extratropical (a) North Atlantic and (b) North Pacific (see Fig. 4). Contour interval 10%. Heavy and light stippling indicate correlation values larger than 30% and less than −30%, respectively. The zonally averaged values for individual winter seasons have been removed from the height data prior to the analysis.

The leading SST pattern for the North Pacific (NP1, see Fig. 4b) exhibits a higher degree of zonal asymmetry than the NA1 pattern. Most notable in the Pacific pattern is the east–west oriented dipole in the eastern half of the basin. This feature is only weakly correlated with SST fluctuations in the equatorial Pacific. The absence of any significant signal in the tropical sector of Fig. 4b cannot be attributed to the application of the bandpass filter prior to the RPC analysis, since the corresponding RPC pattern based on unfiltered SST data (not shown) is almost identical to Fig. 4b. A pattern similar to Fig. 4b appears as the second nonseasonal EOF of the observed SST field for the tropical and North Pacific (Weare et al. 1976, Fig. 8), as the first RPC of the observed North Pacific SST field for all months of the year (Walsh and Richman 1981, Fig. 4), and as the first EOF of the SST field for the extratropical North Pacific (WSJ, Fig. 1). Except for some displacements of the anomaly centers, the same phenomenon is also evident in the teleconnection patterns using locations north of Hawaii and off the U.S. West Coast as the reference grid points (WJ, Fig. 4). Comparison between the essential features in Figs. 4b and 3b suggests that the characteristic SST pattern accompanying ATM2 bear some resemblance to the principal mode of oceanic variability in the North Pacific. However, there exists a notable displacement between the positive extrema appearing north of Hawaii in Figs. 3b and 4b.

The distribution of correlation coefficients between the local 515 mb height and the temporal coefficients for NP1 is displayed in Fig. 5b. This pattern indicates that warm SST anomalies near 40°N, 150°W and cold anomalies near 30°N, 130°W are associated with positive height perturbations over the northeast quadrant of the North Pacific, and negative perturbations over the central and eastern subtropical Pacific as well as the Labrador Peninsula. The positions of extrema appearing in the eastern Pacific sector of Fig. 5b are in fair agreement with those in ATM2 (Fig. 2b). However, the centers over Labrador and the subtropical Atlantic in Fig. 5b are shifted considerably east of the corresponding centers in Fig. 2b. The one point teleconnection analysis to be presented in the next section (see Fig. 8) indicates that the atmospheric response exhibits some sensitivity to the precise location of the SST anomaly in the Pacific. The differences between the atmospheric patterns in Figs. 2b and 5b are evidently related to spatial displacements of the anomaly

centers in the accompanying SST fields (compare Figs. 3b and 4b).

In summary, by first identifying the principal atmospheric spatial modes and then relating these modes to the prescribed SST forcing (see section 3); and by first documenting the prominent oceanic anomalies and then associating such anomalies to the atmospheric response (this section); we have arrived at essentially the same conclusion; i.e., that there exists a nearly one-to-one correspondence between recurrent circulation anomalies in the model atmosphere and well-organized SST patterns imposed in the extratropics. These findings also indicate the geographical locations of the SST perturbations which are most correlated with the ATM1 and ATM2 modes. It remains to be demonstrated that the SST forcing at these oceanic sites accounts for maximal spatially integrated variability of the 515 mb height field. We proceed to address this issue in the following section.

5. Locations of SST anomalies explaining maximal atmospheric variance

The SST sites as identified using the RPC and cross-correlation analyses in the previous two sections constitute only a small fraction of the total area of the World Oceans. In order to ascertain that we have not overlooked any other maritime regions which might exhibit comparably strong correlations with the model atmosphere, an exhaustive survey of the covariability between the atmosphere and ocean has been conducted by computing every element of the matrix $r_{ij} = r(SST_i, Z_j)$, where r denotes the temporal correlation coefficient between the pair of time series listed in the parentheses, SST_i are the SST anomalies at any grid point i in the stippled region in Fig. 1, and Z_j are the corresponding 515 mb height anomalies at any grid point j between 20°N and 79°N. All oceanic and atmospheric anomalies are based on seasonally averaged values for 29 individual winters. A useful measure of the strength of the atmospheric signal associated with the SST input at the ocean point i would be the following index

$$I_i = \sum_j r_{ij}^2 \cos\theta_j$$

$$\text{for all } j \quad \text{with} \quad r_{ij}^2 > 0.1.$$

Here θ_j is the latitude of the atmospheric grid point j. This index may be interpreted as the areal sum of the cosine latitude-weighted fractions of atmospheric variance attributable to the SST fluctuations at i. The summation process has been performed over those points j with $|r_{ij}| > \sqrt{0.1} = 0.32$, so that only those atmospheric sites with correlation values surpassing the 90% significance criterion are considered here. Experimentations with different values for this threshold indicate that the spatial behavior of I_i is not sensitive to the criterion chosen here. The distribution of I_i over much of the Atlantic and Pacific Basins is displayed in Fig. 6. Maxima in this pattern signify strong covariability between local SST variations and the atmospheric flow pattern.

In the Atlantic sector, maximum values of I are found along a band extending eastward from the coasts of Nova Scotia and Newfoundland to about 30°W, as well as along another zonal belt located at 20°N from 60°W to the north African coast. Another prominent feature of note is the extremum lying across the subtropical South Atlantic. A local maximum in the Bermuda region is also discernible. In the Pacific sector, the most notable features in Fig. 6 are the maximum extending southwestward from the U.S. west coast to the subtropics, and the belt of high index values spanning from north of Hawaii to the tropical western Pacific. The values along the equatorial Pacific are seen to be considerably lower than those associated with the midlatitude features mentioned above. Nearly all of the maxima in I are collocated with extrema in the RPC patterns for NA1 and NP1 (Fig. 4), and with those maritime sites most correlated with the atmospheric ATM1 and ATM2 modes (Fig. 3). The results presented in Fig. 6 hence offer independent evidence that, among all the grid points situated in the Atlantic and Pacific, the SST anomaly regions identified in the sections 3 and 4 indeed account for maximal variability of the model atmosphere.

The sensitivity of the atmospheric response to the precise location of the imposed SST forcing in a general region may be delineated by mapping the values of r_{ij} for various SST base points i situated in that region. In the course of this study, a large number of such "one-point teleconnection charts" have been scrutinized. We shall only present here a highly condensed set of correlation charts which exhibit the strongest and most interesting atmospheric signals. In Fig. 7 are shown the distributions of the temporal correlation coefficients between wintertime 3-month mean 515 mb height at individual grid points and the corresponding SST anomalies averaged over selected 9° (latitude) by 15° (longitude) rectangles in the North Atlantic. Panels (a)–(c) of this figure are based on three neighboring rectangles located progressively east of the coasts of Newfoundland and Nova Scotia. The reference SST locations for panels (d)–(f) lie along the 22.5°N latitude and are placed directly south of the rectangles chosen for the first three panels. Similarly, the correlation charts based on selected SST rectangles in the North Pacific are displayed in Fig. 8. The first three maritime sites examined in the latter figure are situated north of Hawaii, and are linked to each other along an axis with a southwest-to-northeast orientation. The remaining three panels in Fig. 8 are based on a similarly oriented set of rectangles located west of Baja California. The position of the centroid of the SST rectangle used for constructing a given teleconnection chart is indicated by a solid dot on the same chart. Such positions are also collectively plotted in Figs. 3, 4 and 6.

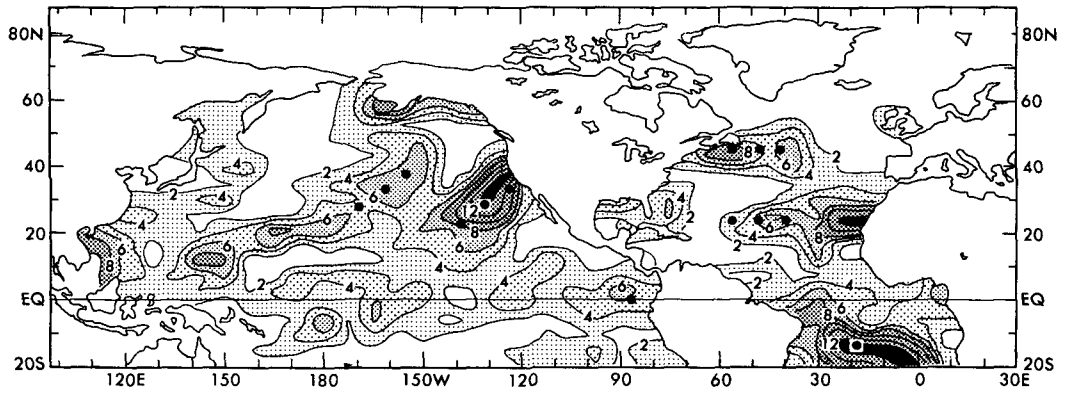

FIG. 6. Distribution of the index I (see definition in section 5), a measure of the fraction of spatially integrated extratropical 515 mb height variance explainable by SST fluctuations at individual grid points. Contour interval 2. Large values of this index are depicted by stippling of increasing density. The computations were based on three-month averages for the northern winter season. The zonally averaged values for individual winter seasons have been removed from the height data prior to the analysis. The solid dots indicate the locations of the reference SST sites selected for constructing teleconnection charts in the latter part of this study (see also Figs. 3 and 4).

The rationale for choosing the particular reference SST sites for teleconnection analysis is evident from the spatial relationships of the solid dots with the principal features in the latter figures; i.e., these rectangles correspond closely to the sites of maximum correlation with the ATM1 and ATM2 atmospheric patterns (Fig. 3), the extrema in the NA1 and NP1 patterns (Fig. 4), as well as maxima in the index I (Fig. 6). It is worth noting here that some of the selected SST sites examined in Figs. 7 and 8 are also nearly coincident with those investigated in various observational studies, such as those by Palmer and Sun (1985), WJ and WSJ.

Inspection of the panels in a given column of Figs. 7 and 8 reveals that SST anomalies in neighboring rectangles are correlated with similar atmospheric patterns. However, the strength of the correlations and the details of the correlation pattern exhibit some sensitivity to the position of the reference SST point. The patterns in the left column of each figure bear some resemblance to those displayed in the right column of the same figure, except for a sign reversal. The latter result is a consequence of the out-of-phase relationships between the SST fluctuations at two groups of sites described in each figure; i.e., note the dipole-like structures in the NA1 and NP1 patterns (Fig. 4). Comparison among the panels in Figs. 7 indicates that the characteristic circulation pattern in the Atlantic/European sector, which exhibits many similarities to the ATM1 mode (Fig. 2a), is most correlated with the SST rectangle centered at 45°N, 56°W (see Fig. 7a). This particular Atlantic site is hereafter referred to as ATL. The detailed structure of the atmospheric teleconnection patterns appears to be more sensitive to the specific locations of the reference Pacific sites (see Fig. 8) than to the Atlantic sites (Fig. 7). Among the charts presents in Fig. 8, the teleconnection pattern accompanying SST anomalies at 31.5°N, 161°W (hereafter referred to as PAC, see Fig. 8b) bears the strongest resemblance to the ATM2 pattern (Fig. 2b). This finding is consistent with the collocation of the PAC site with the positive extremum appearing in the SST correlation chart associated with ATM2 (Fig. 3b). On the other hand, panels (a), (d), (e) and (f) in Fig. 8, which correspond to reference sites located near the extrema of the NP1 pattern (see Fig. 4b), are rather similar to the 515 mb height correlation chart associated with NP1 (see Fig. 5b).

The simulated teleconnection pattern associated with the ATL site (Fig. 7a) bears a considerable spatial resemblance to its observed counterpart (WJ, Fig. 7). There also exists a one-to-one correspondence between the principal correlation centers appearing in the model response to SST variations at PAC (Fig. 8b) and those in the observed pattern (WJ, Fig. 6), with the exception that the simulated extremum over the Labrador Peninsula is displaced to the east of the observed feature. We shall henceforth investigate the behavior of different parameters of the model atmosphere in relation to the SST forcing at ATL and PAC.

6. Regression patterns associated with SST variations at ATL

In order to document the nature of various atmospheric signals related to SST fluctuations at the maritime sites identified in the previous section, linear regression coefficients have been computed between the SST time series at these particular sites and the time series of selected model variables at individual grid points. The hemispheric distributions of such coefficients, hereafter referred to as regression patterns, not only describe the *horizontal structure* of the model response to the SST conditions at the reference site, but also provide important information on the *amplitude*

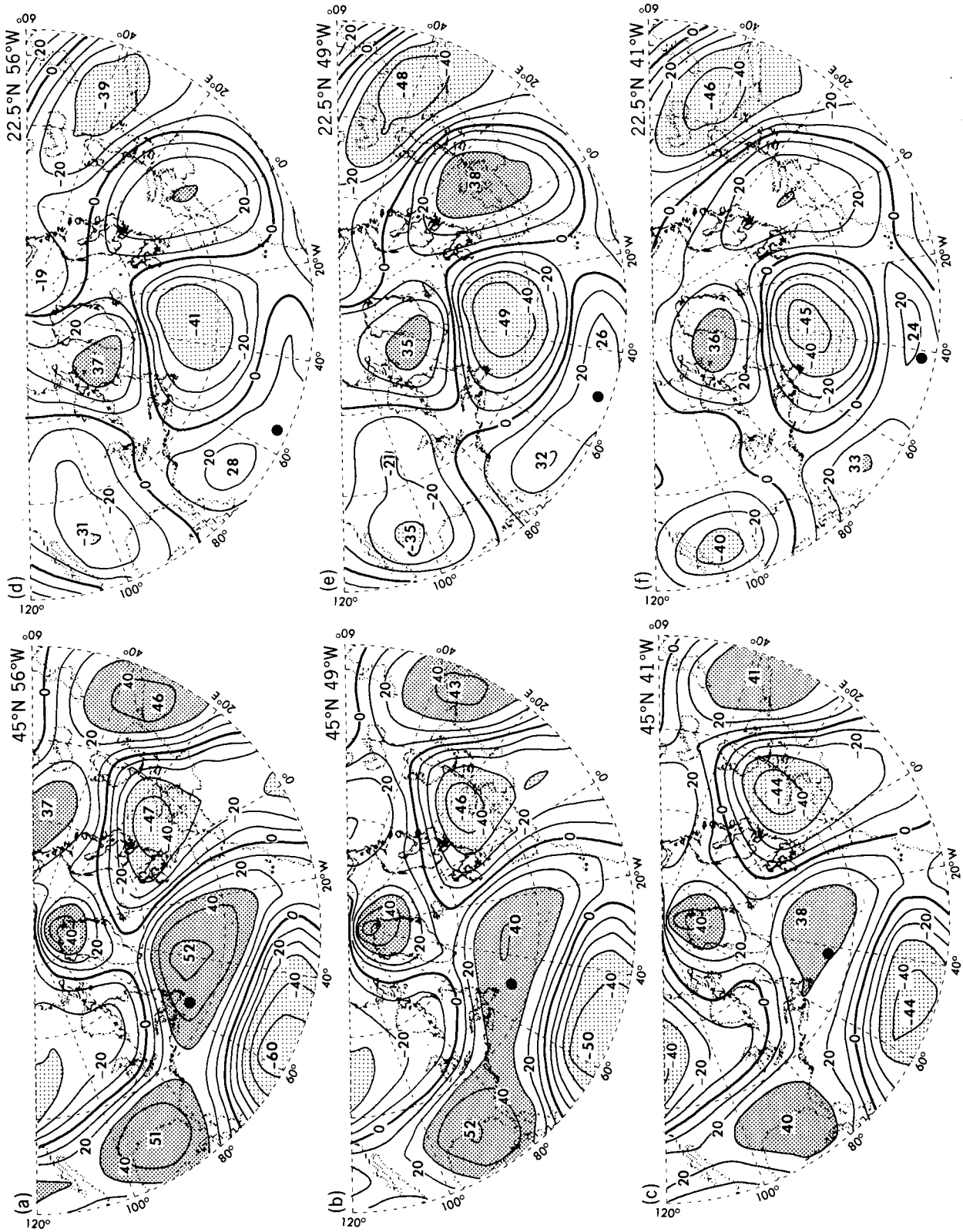
45°N 56°W
45°N 49°W
45°N 41°W
22.5°N 56°W
22.5°N 49°W
22.5°N 41°W
(a)
(b)
(c)
(d)
(e)
(f)

of the model signal per unit SST forcing. A similar method has been used by Nakamura et al. (1987) to study the observed circulation patterns and energetics associated with various teleconnection indices. The regression patterns with reference to the SST anomalies at the ATL and PAC sites (see definitions at the end of section 5) will be presented in the present and the next sections, respectively. All regression values shown here are based on 3-month averages for 29 individual winters.

In Fig. 9 are shown the horizontal distributions of the regression coefficients between SST perturbations averaged over the 9° (latitude) × 15° (longitude) rectangle centered at 45°N, 56°W (i.e., the ATL site), and the geopotential height variations for individual grid points at (a) 205, (b) 515 and (c) 990 mb. The statistical significance of the coefficients displayed here has been estimated using the procedure outlined by Nakamura et al. (1987, section 3), which entails application of the F-test to the ratio of the variance attributable to the linear regression versus the residual variance. Those values in Fig. 9 (as well as subsequent regression patterns in Figs. 10–14) with F-ratios surpassing the 90%, 95% and 99% significance levels are indicated in the corresponding panels by stippling of increasing density. In each panel shown in Figs. 9–15, the location of the centroid of the reference SST site is indicated by a solid dot. The spatial similarities among the three panels in Fig. 9 suggest an equivalent barotropic response of the model atmosphere to the prescribed SST forcing at ATL. A well organized wave train is evident in each of these regression patterns, with warm SST anomalies at ATL being accompanied by negative height anomalies over the central subtropical Atlantic and the North Sea region, and positive height anomalies just downstream of ATL as well as the Caspian Sea region. This configuration of anomaly centers in the geopotential height field is essentially the same as those appearing in the charts of normalized correlation coefficients shown in Figs. 2a, 5a and 7a. The regression values at most of these anomaly centers are significant at the 95% level. The model-simulated results in Fig. 9 bear a considerable resemblance to the observed composite patterns of the 500 mb height and sea level pressure fields corresponding to anomalous SST episodes in the ATL region during the 1951–1980 period, as documented by Palmer and Sun (1986, Figs. 10–12). For the positive North Atlantic center in Fig. 9, the amplitude of the height response is seen to increase monotonically from about 20 m per °C of SST forcing near the sea level, to about 30 and 40 m per °C in the middle and upper troposphere, respectively. The magnitude of the model response is comparable to that inferred from the composite maps presented by Palmer and Sun using observational data. It is worth noting that the present simulation appears to yield stronger amplitudes than the experiment conducted by Palmer and Sun using the GCM at the U.K. Meteorological Office. These authors reported a model sensitivity of about 20 m of geopotential height at 500 mb per °C of SST anomaly (see their Figs. 2a and 8a).

The regression maps of (a) SST, (b) precipitation rate, and (c) sum of latent and sensible heat flux from the ocean versus SST fluctuations at the ATL site, are displayed in Fig. 10. The pattern in panel (a) illustrates the tendency for the temperature at the ATL region to vary in opposition to SST in the western and central subtropical Atlantic, as was noted previously in Figs. 3a and 4a. The most prominent feature in the precipitation chart (Fig. 10b) is the zonally elongated belt of negative values spanning across the Atlantic at 35°–40°N. Warm SST anomalies at ATL are hence associated with suppressed rainfall in a broad region located 5–10° of latitude to the south of the forcing region. The amplitude of the model response (0.04–0.1 cm day^{-1} per °C of SST forcing) may be compared with the climatological precipitation rate of 0.3–0.5 cm day^{-1} in this region (see Manabe and Holloway 1975, Fig. 13; and Lau 1985, Fig. 6a). The precipitation anomaly at the ATL site itself is much weaker. Small positive regression values of rainfall rates prevail in the region lying to the north of ATL. The regression pattern for total heat flux across the air–sea interface (Fig. 10c) is characterized by a dipole with negative values (i.e., below normal heat flux from the ocean to the atmosphere) south of ATL, and positive values in regions farther north. The regression values shown in Fig. 10c (10–20 W m^{-2} per °C) are approximately 5%–10% of the climatological heat transfer rate over the western Atlantic (see Bunker 1976).

The results in Fig. 10 indicate noticeable displacements of the precipitation and oceanic heat flux anomaly centers from the ATL site. Since the intensity of both the rainbelts and the air–sea heat exchange in the middle latitudes is closely related to the local behavior of transitory synoptic disturbances, we would expect the trajectory and frequency of such transient phenomena to be also affected by extratropical SST anom-

FIG. 7. Distributions of the temporal correlation coefficients (in percent) between 515 mb height at individual grid points and the SST values averaged over 9° (latitude) × 15° (longitude) rectangles located in the Atlantic and centered at (a) 45°N, 56°W, (b) 45°N, 49°W, (c) 45°N, 41°W, (d) 22.5°N, 56°W, (e) 22.5°N, 49°W and (f) 22.5°N, 41°W. Contour interval 10%. Heavy and light stippling indicate correlation values larger than 30% and less than −30%, respectively. The computations were based on three-month averages for the northern winter season. The zonally averaged values for individual winter seasons have been removed from the height data prior to the analysis. The centroid of the reference SST rectangle for each chart is indicated in the corresponding panel by a solid dot. These locations are also depicted in Figs. 3, 4, and 6.

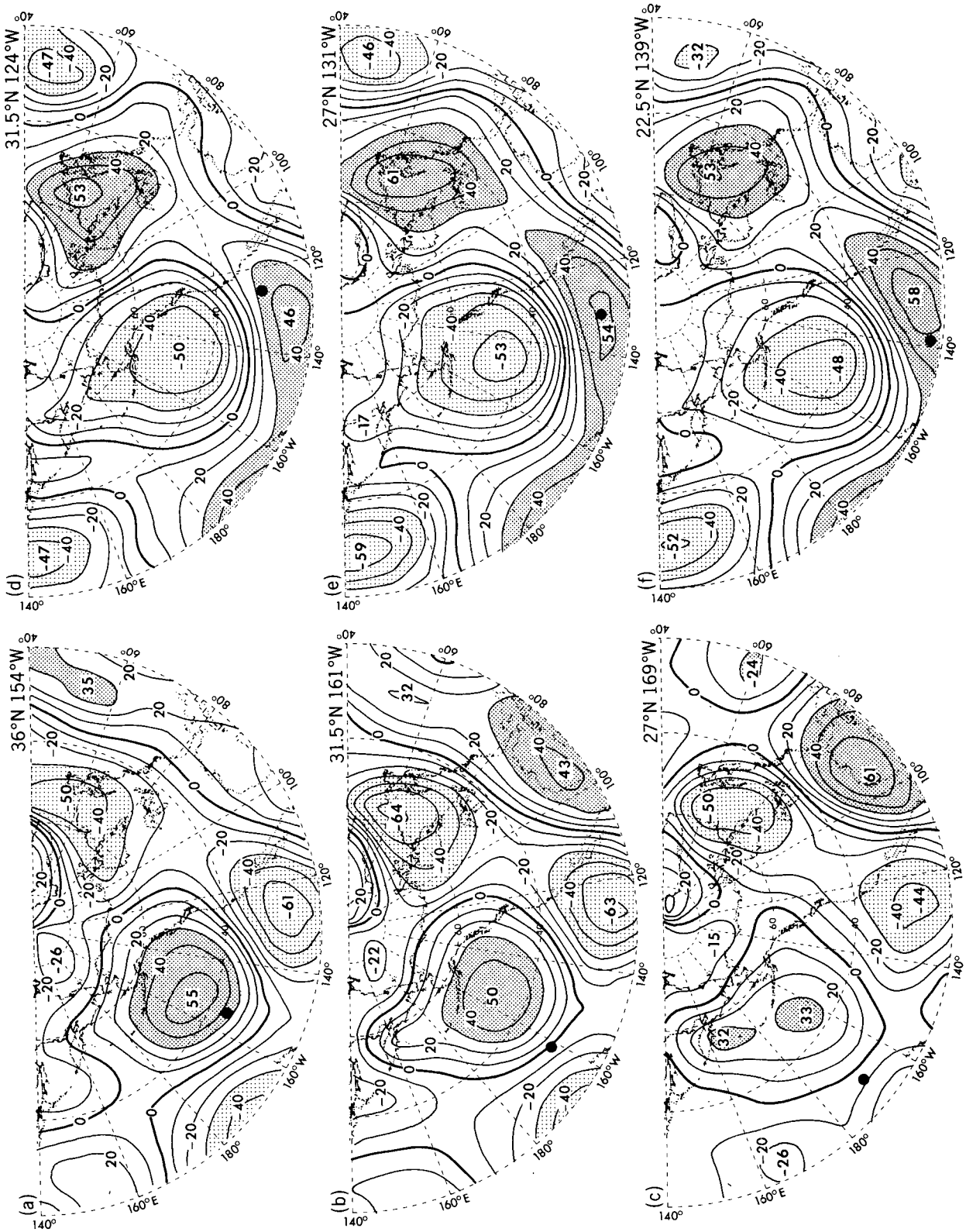
(a) 36°N 154°W
(b) 31.5°N 161°W
(c) 27°N 169°W
(d) 31.5°N 124°W
(e) 27°N 131°W
(f) 22.5°N 139°W
140°
160°E
180°
160°W
140°
120°
100°
80°
60°
40°

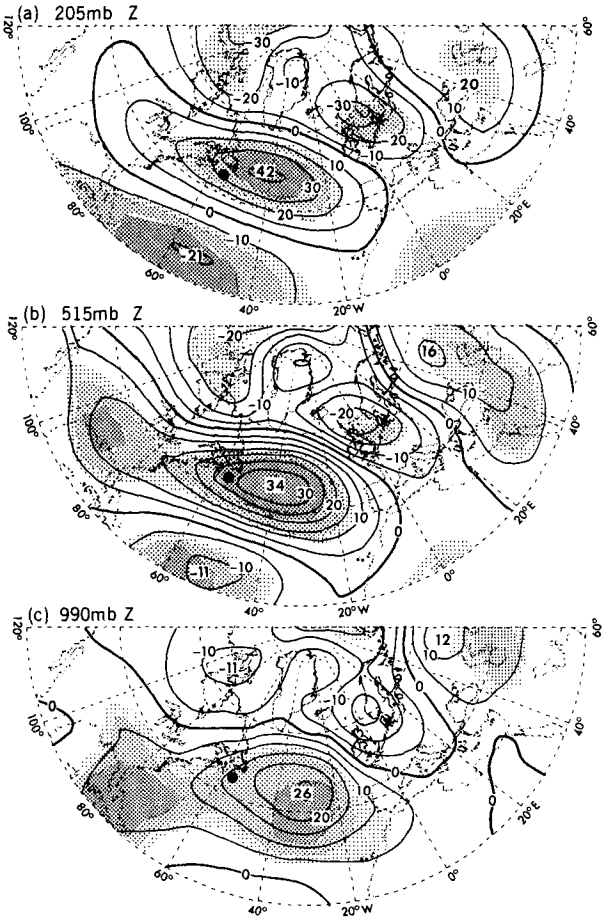

FIG. 9. Distributions of the linear regression coefficients between SST variations at the ATL site (i.e., the 9° × 15° rectangle centered at 45°N, 56°W, indicated by the solid dot in individual panels) and grid point values of geopotential height at (a) 205, (b) 515, and (c) 990 mb. Contour intervals are 10 m per °C for panel (a), and 5 m per °C for panels (b) and (c). Significant regression values at the 90%, 95% and 99% levels are indicated by light, medium, and heavy stippling, respectively. The computations were based on 3-month averages for the northern winter season.

alies. The observational studies by Blackmon (1976) and Blackmon et al. (1977) have demonstrated that the most active synoptic scale wintertime fluctuations in the Northern Hemisphere occur along zonally elongated "storm tracks" over the North Atlantic and the North Pacific at about 45°N. These and subsequent works revealed that the properties of disturbances within these storm tracks may be inferred from the spatial patterns of temporal variance and covariance circulation statistics. In particular, it is known that the axes of the climatological oceanic storm tracks are coincident with the maxima in the variance of the time-filtered meridional wind component $\overline{v'v'}$ (Blackmon et al. 1977, Fig. 5b), and with the maxima in the meridional heat transport $\overline{v'T'}$ by synoptic scale eddies (Blackmon et al. 1977, Fig. 11b). Lau (1988) has presented further observational evidence that the month-to-month changes in the storm track behavior may be delineated by the variability of such second-moment statistics computed for individual winter months. In the present study, we shall use the $\overline{v'v'}$ and $\overline{v'T'}$ statistics for a given month to infer the position and intensity of the storm tracks for that month. These statistics have been computed using unfiltered daily time series for

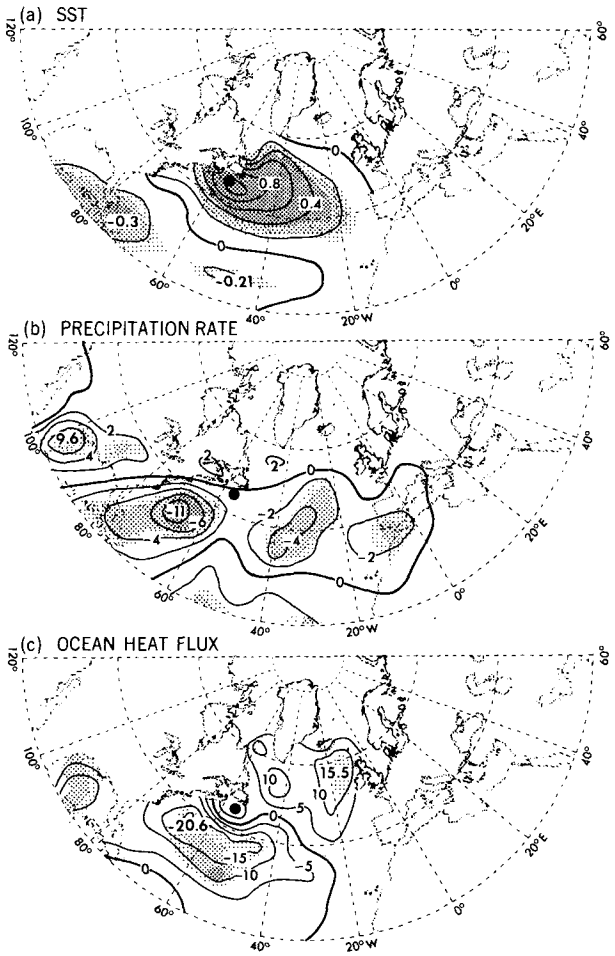

FIG. 10. As in Fig. 9, except for regression of the SST time series at ATL with grid point data for (a) sea surface temperature, contour interval 0.2°C per °C, (b) precipitation rate, contour interval 2×10^{-2} cm day^{-1} per °C, and (c) sum of latent and sensible heat flux from the ocean to the atmosphere, contour interval 5 W m^{-2} per °C.

FIG. 8. As in Fig. 7, except for reference SST rectangles located in the North Pacific and centered at (a) 36°N, 154°W, (b) 31.5°N, 161°W, (c) 27°N, 169°W, (d) 31.5°N, 124°W, (e) 27°N, 131°W and (f) 22.5°N, 139°W.

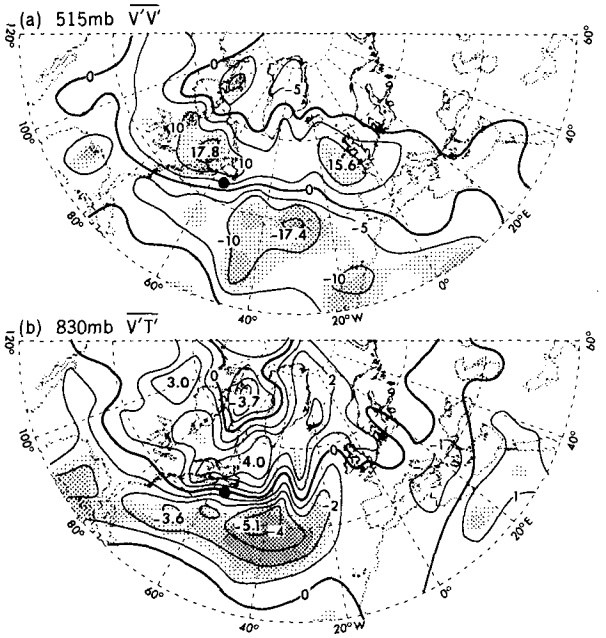

FIG. 11. As in Fig. 9, except for regression of the SST time series at ATL with grid point data for (a) transient eddy variance of the meridional wind $\overline{v'v'}$ at 515 mb, contour interval 5 m^2 s^{-2} per °C, and (b) meridional heat flux by transient eddies $\overline{v'T'}$ at 830 mb, contour interval 1°C m s^{-1} per °C. The transient eddy statistics were computed using departures of unfiltered daily data from the monthly mean values.

each month of the 360-month integration, and hence include contributions of eddies with temporal periods ranging from two days to a month. The overbars in $\overline{v'v'}$ and $\overline{v'T'}$ therefore denote time averaging over a month, and the primes represent deviations of daily data for a given month from the mean for the same month. The mean values for a given winter were then obtained by averaging these monthly statistics for the three months within that season. The second-moment statistics compiled in this manner encompass a broader range of time scales than the bandpass (2.5–6 d) filtered statistics examined by Blackmon and collaborators. Nonetheless, the climatological charts of $\overline{v'v'}$ and $\overline{v'T'}$ obtained here (not shown) are also characterized by zonally elongated maxima in the oceanic storm track regions. Hence the fluctuations with periods of several days still make substantial contributions to the circulation statistics examined here.

Figure 11 shows the wintertime regression patterns of (a) $\overline{v'v'}$ at 515 mb and (b) $\overline{v'T'}$ at 830 mb versus the seasonally averaged SST fluctuations at ATL. Both panels of this figure indicate that warm SST anomalies at ATL are accompanied by reduced meridional wind variance and eddy heat transports south of the reference site, and by enhanced eddy activities farther north. The ATL site itself lies along the nodal line of these dipole-like patterns, and corresponds to anomalous divergence of meridional eddy heat fluxes. Since the climatological position of the Atlantic storm track in the model atmosphere also corresponds to the zero contours in Fig. 11 (see Lau and Nath 1987, Fig. 1f), above-normal temperatures at ATL are therefore associated with a northward displacement of the Atlantic storm track, and vice versa. A similar conclusion has been reached by Palmer and Sun (1985) on the basis of model experiments with idealized anomalies in the ATL region. It is seen that the region of increased eddy activity is coincident with westerly wind anomalies in the seasonally averaged flow pattern, as may be deduced from Fig. 9 using the geostrophic relationship; whereas suppressed high-frequency fluctuations are locally accompanied by easterly anomalies in the seasonal mean circulation. The regression patterns for transient eddy activity (Fig. 11) generally exhibit a positive spatial correlation with the patterns for precipitation (Fig. 10b) and ocean heat flux (Fig. 10c). It is also evident from these figures that the extrema in the regression maps for transient eddy statistics are sites of strong meridional gradients in the imposed SST anomaly (see Fig.

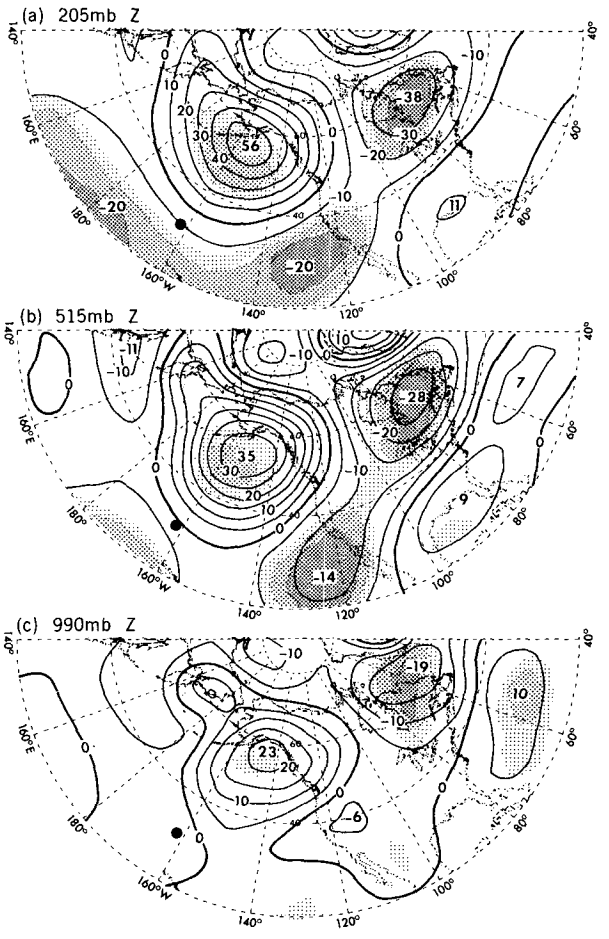

FIG. 12. As in Fig. 9, except for regression versus the SST variations at the PAC site (i.e., the 9° × 15° rectangle centered at 31.5°N, 161°W, indicated by the solid dot in individual panels).

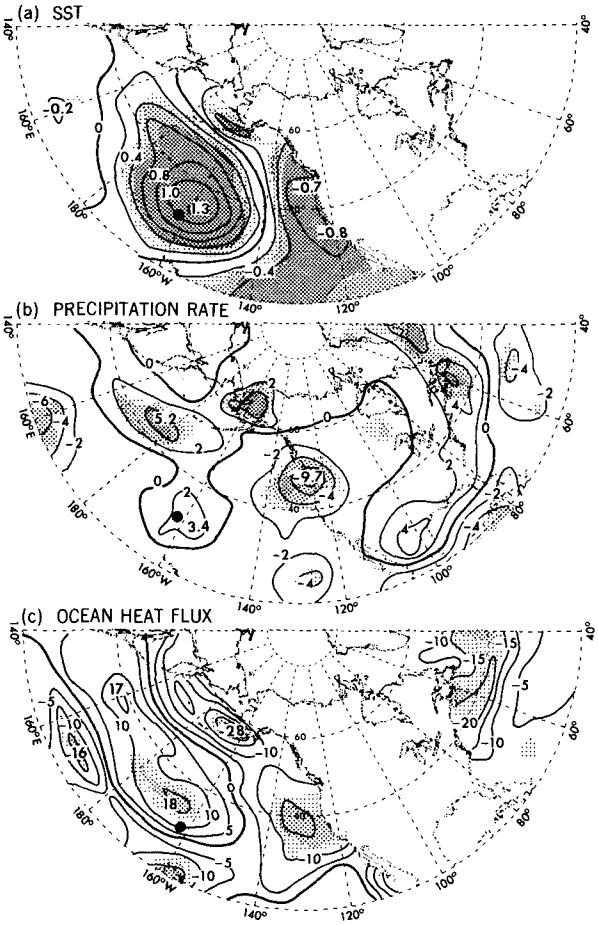

FIG. 13. As in Fig. 10, except for regression versus the SST variations at the PAC site (near 31.5°N, 161°W, see solid dots in individual panels).

10a). The significance levels of the regression coefficients for the precipitation, ocean heat flux, and transient eddy fields are seen to be lower than those for the geopotential fields shown in Fig. 9.

7. Regression patterns associated with SST variations at PAC

We next turn our attention to the model response to oceanic changes in the PAC site near 31.5°N, 161°W. The regression patterns corresponding to this SST site for geopotential height at various tropospheric levels are displayed in Fig. 12. The height anomalies associated with the SST forcing at PAC are also characterized by an equivalent barotropic structure. The chain of alternating high and low pressure centers, noted previously in Figs. 2b and 8b, are apparent in the regression maps presented here. The spatial configuration of the anomaly centers in relation to the PAC site exhibits some notable differences from the corresponding pattern for the ATL site (Fig. 9). The principal center over the Gulf of Alaska is displaced to the north of the PAC anomaly by 25° of latitude, so that the PAC site itself is locally associated with weak changes in the height field. On the other hand, the principal height anomaly center over the North Atlantic is displaced only slightly to the east of the ATL site, so that the SST forcing lies in a region with strong height changes. The amplitudes of individual extrema in Fig. 12 are similar to those for the ATL site (see Fig. 9). The magnitude of the Gulf of Alaska center at 205 mb (about 50 m per °C of SST forcing) is somewhat larger than the corresponding value reported by Pitcher et al. (1988, Fig. 3c) for their GCM experiment with a cold anomaly in the North Pacific.

The regression coefficients between the forcing at PAC and (a) SST, (b) precipitation rate, and (c) total heat flux from the ocean, are presented in Fig. 13. The corresponding regression charts for $\overline{v'v'}$ at 515 mb and $\overline{v'T'}$ at 830 mb are shown in Fig. 14. The east–west seesaw in the North Pacific SST field mentioned in sections 3 and 4 is again evident in Fig. 13a. Recalling that the positive extremum appearing in the NP1 pattern (Fig. 4b) is actually located northeast of the PAC site, we note a similar dislocation of the PAC site from the maximum in the regression chart for the SST field (Fig. 13a). Cold SST anomalies off the west coast of North America are associated with below-normal precipitation in that area (Fig. 13b). The other significant feature in the precipitation chart is the elongated extremum extending northeastward from about 40°N,

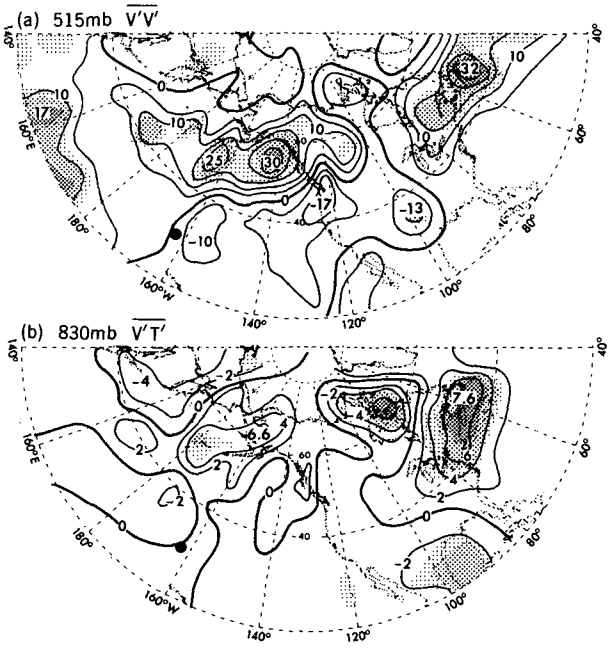

FIG. 14. As in Fig. 11, except for regression versus the SST variations at the PAC site (near 31.5°N, 161°W, see solid dots in individual panels). Contour interval for panel (b) is 2°C m s^{-1} per °C.

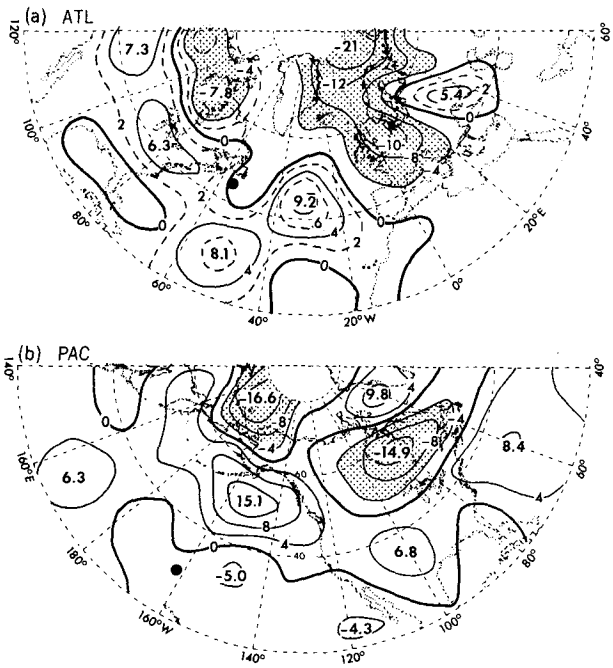

FIG. 15. Distributions of the regression coefficients between grid point values of geopotential height tendency due to transient eddy vorticity fluxes and SST variations at the (a) ATL and (b) PAC sites. Contour interval 4×10^{-5} m s^{-1} per °C. Stippling indicates values less than -4×10^{-5} m s^{-1} per °C. The computations were based on 3-month averages for the northern winter season. The locations of the reference SST rectangles are indicated by solid dots in the corresponding panels.

160°E to the Aleutian Islands and the Alaskan Peninsula. The latter feature is nearly collocated with anomalies of the same polarity in meridional wind variance and poleward eddy heat transport (Fig. 14). It is seen that SST anomalies in the Pacific Basin tend to be positively correlated with the local heat supply from the underlying ocean (Fig. 13c).

The most significant feature over the Pacific in the regression maps for transient eddy statistics (Fig. 14) is the association of warm SST anomalies at PAC with the northeastward excursion of the Pacific storm track from its climatological position (see Lau and Nath 1987, Fig. 1f), which would result in more frequent intrusion of transient disturbances to western Canada and Alaska. These sites of increased eddy activity are characterized by enhanced horizontal gradients of the SST anomaly field (Fig. 13a).

8. Role of transient eddy forcing in the seasonally averaged response

The evidence presented in the regression maps for transient eddy statistics (Figs. 11 and 14) indicates that systematic realignments of the oceanic storm tracks occur during anomalous SST episodes in the middle latitudes. Since the most vigorous transports of vorticity and heat in the extratropics are known to take place within the storm tracks (e.g., see Blackmon et al. 1977 and Lau 1978), one would expect the SST anomalies at ATL and PAC to exert a considerable influence on the seasonal mean circulation by modulating the convergence patterns of transient eddy fluxes. The recent observational study by Lau (1988) confirms that the intermonthly variations of the barotropic forcing by synoptic scale disturbances, as delineated by eddy-induced geopotential height tendencies, are positively correlated with the monthly averaged flow pattern. In examining the origins of atmospheric variability on monthly and seasonal time scales, one must hence take into consideration the role of the eddy transfer of vorticity. In this section, we shall evaluate the circulation changes associated with redistributions of the eddy vorticity fluxes resulting from the storm track displacements noted in Figs. 11 and 14. The geopotential tendency method outlined in Lau (1988) has been adopted to illustrate the effects of variations in the eddy barotropic forcing on the mean seasonal model response. For each individual winter season, the geopotential height tendency may be approximated as

$$\frac{\partial z}{\partial t} = \frac{f}{g} \nabla^{-2} \pi \tag{1}$$

where

$$\pi = \frac{1}{a^2 \cos\theta} \left(\frac{\partial}{\partial \theta} \frac{1}{\cos\theta} \frac{\partial}{\partial \theta} \cos^2\theta - \frac{1}{\cos\theta} \frac{\partial^2}{\partial \lambda^2} \right) \overline{u'v'} + \frac{1}{a^2 \cos^2\theta} \frac{\partial^2}{\partial \lambda \partial \theta} \cos\theta \, (\overline{u'u'} - \overline{v'v'}) \tag{2}$$

is the forcing due to convergence of vorticity transports by the transient eddies in the same winter. Here a is the radius of the earth, f the coriolis parameter, g the gravitational acceleration, and λ, θ are the longitude and latitude, respectively. As in the previous two sections, the transient eddy statistics $\overline{u'u'}$, $\overline{v'v'}$, and $\overline{u'v'}$ for the entire globe have been computed for each winter month using unfiltered daily data. These monthly quantities were then averaged to form seasonal averages for individual winters. The inverse Laplacian operation in Eq. (1) has been performed using two independent methods. The first procedure entailed the decomposition of the eddy forcing term into spherical harmonics and then execution of the inverse Laplacian in the spectral domain. The second approach made use of the subroutine PWSSSP in the NCAR software library to obtain the solution of the finite-difference version of Eq. (1). It is seen that these two techniques yield essentially the same results. It needs to be emphasized here that only the barotropic forcing associated with eddy vorticity fluxes have been treated in the present formulation. We have not taken into account the forcing due to variability in heat transports by the active baroclinic eddies along the storm tracks.

The regression patterns of the geopotential height tendency at 205 mb versus the SST variations at (a) ATL and (b) PAC are displayed in Fig. 15. The 205 mb level has been chosen for the present diagnosis in view of the finding by Lau and Holopainen (1984) that the eddy-induced height tendency due to barotropic processes attains maximum amplitudes in the upper troposphere, and that vorticity fluxes are much more important than heat fluxes in determining the eddy forcing near the tropopause level. However, it is worth noting that the heat fluxes make a strong contribution to the eddy forcing near the sea level (see Lau and Holopainen 1984, Figs. 3 and 4). The most salient features in Fig. 15a downstream of the ATL site are the chain of extrema located at 45°N, 30°W, the North Sea and the Black Sea. These centers are seen to correspond to, and have the same polarity as, extrema in the seasonally averaged height response downstream of the ATL site (compare Fig. 15a with Fig. 9a). However, such spatial correspondence between the mean height field and its eddy-forced tendency are not as evident at the ATL site itself and the subtropical Atlantic. The observational results presented in Lau (1988, Fig. 12) generally indicate a strong resemblance between the quasi-steady circulation and the height tendency associated with eddies with periods of 2.5–6 days. The relatively weaker correspondence between Figs. 15a and 9a in the present study could partially be a result of the broader range of time scales (2–30 d) included in the variance and covariance statistics used for computing the eddy forcing in Eq. (2).

In the Pacific sector, the diversion of the storm track towards the Alaskan region (Fig. 14) in the presence of warm anomalies at PAC results in positive height tendencies centered at 50°N, 150°W, and negative tendencies in regions farther north and farther south (Fig. 15b). Westerly accelerations of the mean circulation hence prevail in the Bering Strait/Alaskan region, where above-normal eddy activities occur. The nearly in-phase relationship between the extratropical seasonal mean height response and the barotropic eddy forcing, as was hinted in the discussion of the Atlantic patterns, is even more apparent in the Pacific (compare Fig. 15b with Fig. 12a). The characteristic time scale required for the transient eddy vorticity transports to establish height anomalies of amplitudes comparable to the seasonal mean model response, as estimated by the ratio of the representative values in Figs. 9a and 12a to those in Fig. 15, is on the order of 3–4 days. Alteration of storm track behavior and the associated barotropic eddy processes is hence seen to be an efficient pathway for linking the imposed SST forcing in the extratropics to the quasi-stationary atmospheric response. Palmer and Sun (1985) have used Eliassen-Palm vector diagnostics to assess the effects of storm track dislocation in their Atlantic SST experiment, and have similarly pointed out the notable impacts of eddy barotropic forcing on the time-mean state of the model atmosphere.

9. Contribution of prescribed SST anomalies to the amplitude of model variability

We have thus far been mostly concerned with the impact of SST anomalies on the *spatial pattern* of various circulation features. It is also important to assess the extent to which such SST fluctuations contribute to the *amplitude* of the total variability of the model atmosphere on seasonal time scales. In order to determine the incremental variability due to the presence of anomalous oceanic forcing, the temporal variance of the seasonal mean data for the model run with prescribed monthly SST anomalies has been compared with the corresponding statistic derived from a control experiment subjected to the same climatological lower boundary condition every year. The same GCM has been used in both the 10-year control experiment and the 30-year SST anomaly run (see section 2). The variance statistics of the control integration may hence be interpreted as a measure of the "internal variability" of the model at hand.

The distribution of the root-mean-squares (rms) of 515 mb height for the SST anomaly run is shown in Fig. 16a. The ratio of the variance of 515 mb height for the SST anomaly experiment to the corresponding variance for the control run at the same grid point is mapped in Fig. 16b. The values in both panels of Fig. 16 have been computed using seasonally averaged data for winter. The variability of the SST anomaly run attains maximum amplitudes over Alaska, the East Siberian Sea, and the Norwegian Sea, as well as off the Newfoundland coast. The rms values at these sites are 70%–80% of the observed amplitudes (see Blackmon et al. 1984, Fig. 2a). The statistical significance of the variance ratio presented in Fig. 16b may be estimated by application of the F-test (e.g., Panofsky and Brier 1958). Considering the number of degrees of freedom in the numerator and denominator of the ratio (i.e., 28 and 8, respectively), values in Fig. 16b exceeding approximately three would be significant at the 95% level. Inspection of this pattern indicates that the height variability in the SST anomaly run surpasses the internal variability of the model atmosphere at only a few sites of limited extent. Considering that the variance ratio at 5% of the grid points could exceed the 95% confidence level by chance, the significance of the sites of enhanced variability in Fig. 16b is somewhat questionable. Nonetheless, it is worth noting that the maxima over the eastern Atlantic at 40°N, the Norwegian Sea, and the Black Sea are collocated with the extrema in transient eddy forcing accompanying SST variations at ATL (Fig. 15a), while the maximum over Mongolia is nearly coincident with a center of action appearing in ATM1 pattern (Fig. 2a). In the Pacific/North

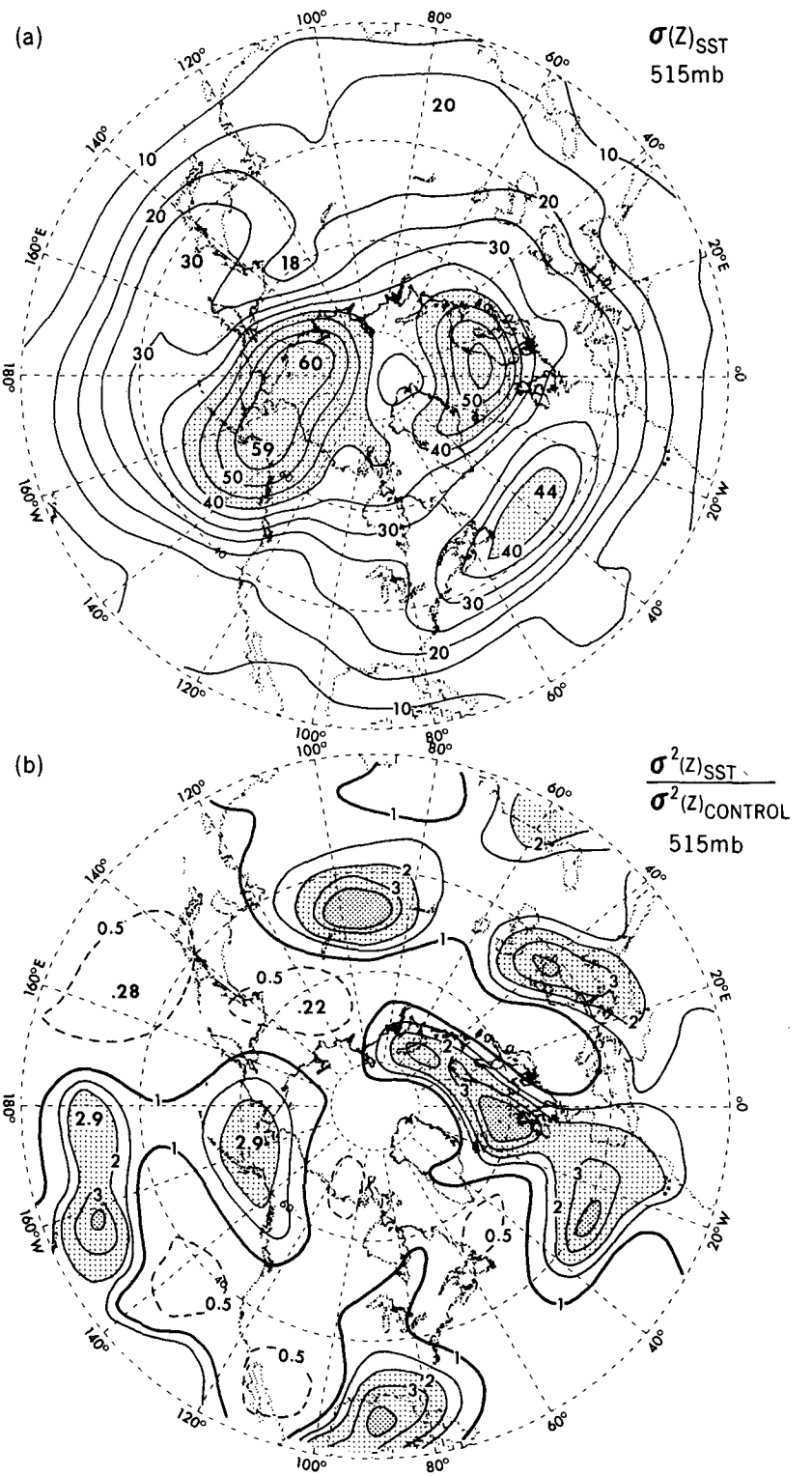

FIG. 16. Wintertime distributions of (a) the root-mean-squares of 515 mb height, as computed using seasonal averages for the 30-year SST anomaly experiment, contour interval 5 m, stippling indicates values larger than 40 m, and (b) ratio of the variance of seasonal means of 515 mb height for the SST anomaly experiment to the corresponding statistic for the control run, isolines of 0.5, 1, 1.5, 2, 3 and 4 are shown, light and heavy stippling indicate values larger than 2 and 4, respectively.

American sector, the maxima in Fig. 16b located just north of Hawaii, in the Bering Sea/Alaskan region, and over the Gulf of Mexico correspond closely to the extrema in the ATM2 pattern (Fig. 2b).

10. Model response to tropical SST anomalies

The primary objective of the present paper is to document the influences of *extratropical* SST variability on the atmospheric circulation. Bearing in mind that the experiment studied here entails the prescription of SST anomalies in both the northern and tropical oceans (see Fig. 1), the circulation features related to SST fluctuations in the *tropics* would also be of interest. Regression maps versus SST variations in the equatorial Pacific (not shown) reveal that the tropical response of the model atmosphere during El Niño events exhibits many of the characteristics described in Lau (1985), who examined model runs with SST changes imposed in the tropical Pacific only. Specifically, diagnoses of the tropical data generated in the present 30-year integration indicate that the oceanic forcing in the El Niño region is strongly correlated with

- east–west seesaws in the sea-level pressure and precipitation fields across the tropical Pacific Basin,
- a zonally symmetric response in the wintertime 205 mb height field along the equatorial belt,
- systematic changes in the strength of the near-surface trade winds and the associated convergence patterns, and
- movement and intensification of the pair of upper tropospheric Pacific anticyclones straddling the equator.

Throughout the entire tropical belt between 15°S and 15°N, the geopotential height variance for the 30-year SST anomaly run is larger than the corresponding statistic for the 10-year control run by a factor of more than 3. The variance ratio in the deep tropics is substantially higher than its counterpart in the middle latitudes (see Fig. 16b). The prescribed SST fluctuations are therefore seen to be much more effective in enhancing the amplitude of atmospheric variability in the tropics than in the extratropical region.

With regards to the extratropical response to changes in the near-equatorial oceans, we recall the result in Fig. 3a indicating a strong relationship between the atmospheric ATM1 mode and the SST anomalies in the subtropical South Atlantic. The SST perturbations at the latter location account for a large portion of the spatially integrated geopotential height variance in the Northern Hemisphere extratropics (see Fig. 6). The midlatitude circulation pattern associated with this maritime site is illustrated in Fig. 17a, which shows the wintertime distribution of temporal correlation coefficients between departures from zonal symmetry of the 515 mb height at individual grid points and the SST averaged over the 9° (latitude) × 15° (longitude) rectangle centered at 13.5°S, 19°W. The centroid of this rectangle is indicated in Figs. 3a, 4a, and 6 by solid dots. The pattern in Fig. 17a bears a strong resemblance to the correlation chart based on the rectangle centered at the ATL (45°N, 56°W) site (see Fig. 7a). The correlation values in the pattern based on the South Atlantic site are slightly higher than those for the ATL rectangle. In understanding the origin of the ATM1 circulation pattern, one must therefore also consider the potential impact of SST anomalies in the tropical Atlantic. The notable correlations in Fig. 17a could result from the direct forcing of the extratropical atmosphere by the tropical Atlantic. If that is the case, it would be of interest to ascertain the relative contributions to the ATM1 pattern from in situ forcing at the midlatitude ATL site and from remote forcing at the tropical Atlantic. One way to address this issue is to compare the output from two additional GCM experiments, one with temporally varying SST forcing confined to the extratropical Atlantic, and the other with month-to-month SST changes being prescribed in the tropical Atlantic only. Alternatively, the association of SST variability at both ATL and the tropical South Atlantic with the same ATM1 pattern could in

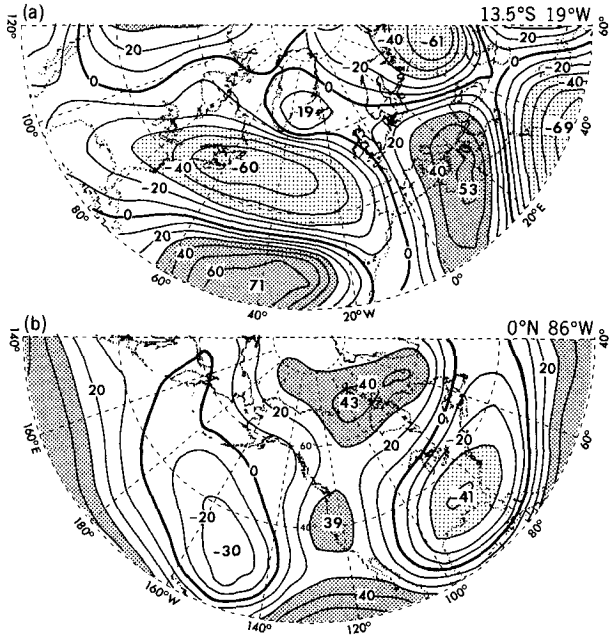

FIG. 17. Distributions of the temporal correlation coefficients (in percent) between 515 mb height at individual grid points and SST variations averaged over 9° × 15° rectangles located in (a) subtropical South Atlantic and centered at 13.5°S, 19°W, and (b) equatorial eastern Pacific and centered at 0°N, 86°W. Contour interval 10%. Heavy and light stippling indicate values larger than 30% and smaller than −30%, respectively. In constructing panel (a), the zonal mean has been removed from the grid point height data. The correlation pattern in panel (b) was based on height data with the zonal mean retained. All computations were performed using 3-month averages for the winter season.

part be explained by the considerable amount of automatic correlation arising from the out-of-phase relationship between the tropical and extratropical SST sites (see Figs. 3a and 4a). Further investigations, perhaps with the aid of coupled ocean–atmosphere models, are necessary to clarify the possible roles of basin-wide internal ocean dynamics, as well as air–sea interaction processes, in forging this apparent link between the conditions of the tropical and midlatitude Atlantic waters.

In the Pacific sector, the SST variations in the El Niño region do not exhibit any strong correlation with the ATM2 pattern (Fig. 3b). The amount of midlatitude atmospheric variance explainable by tropical Pacific SST anomalies is also smaller than that attributed to extratropical anomalies (Fig. 6). The flow pattern accompanying SST changes in the eastern equatorial Pacific is depicted in Fig. 17b, which displays the correlation values between 515 mb height and the SST time series near 0°N, 86°W (see solid dots in Figs. 3b, 4b, and 6). Considering the substantial zonally symmetric component in the observed atmospheric response to oceanic forcing in this region (see WJ, Fig. 2), the zonal mean values of the height field have been retained in the present computation. Correlation charts based on SST rectangles located between the southern American coast and the dateline at the equator (not shown) are similar, but even weaker, than the pattern shown here. The correlations shown in Fig. 17b are generally lower than the corresponding values appearing in the correlation chart based on the PAC (31.5°N, 161°W) site (Fig. 8b). The cumulative evidence presented in this study hence indicates that the prominent mode of simulated atmospheric variability in the North Pacific/North American sector is primarily linked to extratropical SST anomalies in the North Pacific, whereas the oceanic changes in the El Niño region play a relatively minor role. This finding is in accord with the observational results reported in WJ (see their Figs. 2, 6c, and 9), who has similarly noted that SST variability at the PAC site is more effective in specifying atmospheric changes over North America than the remote SST forcing in the equatorial Pacific.

11. Discussion

a. Summary of results

In the present study, the extratropical SST sites which are most strongly related to circulation changes in the model atmosphere have been identified by the following objective techniques:

- searching for locations at which SST variations exhibit the highest temporal correlations with principal atmospheric modes of the GCM under investigation (section 3),
- noting the positions of extrema appearing in the patterns of the leading RPCs for the SST field in individual ocean basins (section 4),
- highlighting maritime regions with SST anomalies explaining substantial fractions of the spatially integrated atmospheric variance (section 5, Fig. 6) and
- "tuning" the locations of the reference SST sites so as to yield the strongest atmospheric teleconnection signals (section 5, Figs. 7 and 8).

The collective evidence gathered from these independent procedures indicate that, among all the grid points situated in the North Atlantic and North Pacific, the SST anomalies imposed at the ATL (near 45°N, 56°W) and PAC (near 31.5°N, 161°W) sites are associated with the most robust and well-defined atmospheric response.

Regression patterns versus the SST variations at ATL and PAC (Figs. 10 and 13) reveal that the midlatitude precipitation anomalies tend to exhibit considerable spatial displacements from the sites of the SST forcing. This result is in sharp contrast to the situation in the tropics, where the most marked precipitation changes are almost coincident with the prescribed SST anomalies (see Lau 1985). The regression maps of transient eddy statistics (Figs. 11 and 14) suggest that the extratropical precipitation response is associated with the reorientation of the wintertime storm tracks during anomalous SST events. The transient disturbances, therefore, play a crucial role in determining the spatial distribution of the latent heat source accompanying midlatitude SST anomalies. Regression charts of the atmospheric heating field due to condensation processes in the extratropical rainbelts (not shown) bear a strong resemblance to the regression patterns of precipitation rate (Figs. 10b and 13b). The anomalous latent heat sources and sinks related to SST changes at ATL and PAC are characterized by a shallow vertical structure, with maximum amplitudes being located near 830 mb. In the Atlantic sector, the transient eddies also exert notable influences on the pattern of latent and sensible heat supply from the underlying ocean (see Fig. 10c).

In addition to their notable relationship with the thermal forcing of the model atmosphere, the high-frequency disturbances are also linked to the quasi-stationary response by virtue of their ability to redistribute vorticity and heat. The computations presented in section 8 indicate that alterations of the convergence patterns of eddy vorticity transports due to storm track displacements are associated with geopotential tendencies which are nearly in phase with the seasonally averaged response. This model finding is consistent with the observational results reported by Lau (1988), who has similarly noted in-phase relationships between the barotropic eddy forcing for individual months and the monthly mean circulation anomalies. In light of the GCM results discussed here, it would be worth in-

vestigating the extent to which the observed storm track variations documented in Lau (1988) are related to the changing SST conditions. The impact of the eddy heat fluxes in the horizontal and vertical directions has not been addressed in this study. Palmer and Sun (1985) have argued that such baroclinic effects cannot be neglected in assessing the full impacts of the eddy forcing.

The model experiment analyzed here highlights the role of the transient disturbances as an intermediary between the imposed SST forcing and the time-mean response. As was pointed out by Palmer and Sun (1985, Fig. 1), the presence of a warm (cold) SST anomaly in a baroclinic zone such as that located off the Newfoundland coast tends to shift the site of strongest horizontal SST gradients poleward (equatorward). Since the synoptic disturbances tend to thrive in regions with the most intense baroclinicity, such shifts in the pattern of SST gradients are accompanied by displacements of the storm tracks from their climatological positions. The dislocations of the storm tracks occur in conjunction with changes in the spatial patterns of the eddy transports and the sources and sinks of latent and sensible heat, which are in turn linked to the anomalous behavior of the seasonally averaged circulation. Changes in the cloud cover accompanying storm track displacements could also lead to systematic alterations in the radiative forcing of the atmosphere. The relative importance of these radiative effects cannot be assessed in the present experiment, since the prescribed cloud cover is dependent on latitude and height only.

b. *Model results for the summer season*

All results shown in the present paper pertain to the northern winter season. The diagnostic procedures outlined in sections 3–5 have also been applied to the model output for the summer months. The latter results (not shown) indicate much weaker relationships between the SST forcing and the summertime circulation in the model atmosphere. The RPCs of the 515 mb height field in the warm season are characterized by small-scale features with considerably less spatial organization than the wintertime patterns. Each of these leading RPC patterns for summer account for about 5%–6% of the hemispherically integrated variance. The fractions of variance explained are hence only half of the corresponding values for winter (see Fig. 2). The extrema appearing in the summertime atmospheric modes do not seem to exhibit any well-defined correlations with nearby SST variations. The spatial patterns of these modes also bear little resemblance to the correlation charts between 515 mb height at individual grid points and the temporal coefficients of leading RPCs of the SST field. The summertime distribution of the index I, which provides for a measure of the spatially integrated atmospheric variance attributable to individual SST sites (see section 5), shows much fewer prominent maxima than its counterpart for the cold season (Fig. 6).

c. *Asynchronous relationships between SST forcing and atmospheric anomalies*

Throughout this study, we have emphasized the simultaneous relationships between the simulated atmospheric behavior and the SST forcing. The apparent success of the present experiment in reproducing some of the observed zero-lag correlation statistics between the atmospheric and oceanic fields suggests that a substantial portion of the observed simultaneous covariability may be attributed to the atmospheric response to oceanic changes. In order to assess the extent to which the correlation characteristics of the ocean-atmosphere system is dominated by the simultaneous relationships noted here, we have explored the nature of lagged correlation coefficients between monthly averaged 515 mb height at individual grid points and SST variations at the ATL and PAC sites. Such correlation statistics have been computed with the SST time series either leading or lagging the height time series by one month. For the ATL site, and with the model output *leading* the SST forcing by one month, the correlation values over the North Atlantic are comparable to the corresponding results based on zero lag. On the other hand, the pattern obtained with the atmospheric time series *lagging* the SST input at ATL by one month exhibits noticeably weaker signals over the North Atlantic than those associated with simultaneous correlations. However, the degree of asymmetry of the correlation statistics with respect to the time lag for the model simulation is considerably weaker than that noted in the observed atmosphere by WJ (see their Fig. 11). For the PAC site, the correlation values computed with model data leading the SST forcing do not differ significantly from the corresponding results obtained with the simulated height anomalies lagging the oceanic changes.

Other observational analyses by Ratcliffe and Murray (1970), Davis (1976), and Palmer and Sun (1985) have also reported that, in addition to the salient simultaneous relationships between anomalies in the atmosphere-ocean system, certain circulation regimes in the real atmosphere tend to lead SST changes in the extratropics. Similarly, WSJ have pointed out that the level of correlation between recurrent atmospheric patterns and the SST *tendency* is even stronger than that between the atmospheric patterns and the simultaneous SST field itself (e.g., see their Fig. 5). Hence the oceanic response to atmospheric forcing is at least as important as the atmospheric response to oceanic forcing in understanding the nature of midlatitude air–sea interaction. The design of the present experiment is such that the ocean has been constrained to follow the observed SST evolution, and is thus not allowed to respond to the varying atmospheric forcing. The

aforementioned weaker degree of asymmetry of the simulated correlation statistics with respect to the temporal lag may be a consequence of the elimination of feedback mechanisms in the ocean. A fully coupled air–sea GCM must be employed to delineate the wide diversity of interactive processes occurring in the extratropical atmosphere and oceans.

Acknowledgments. We wish to thank Dr. S. Manabe and the Climate Dynamics Project at GFDL for providing the GCM used in this study, as well as Dr. A. Oort and the Observational Studies Project for supplying the COADS analyses of the SST field. Mr. T. Delworth and Mr. R. Stouffer have offered invaluable programming assistance in launching the model experiment. The extensive integrations described here have been conducted using the CDC-CYBER 205 machine at the joint National Bureau of Standards-Environmental Research Laboratories (ERL/NOAA) computing facility at Gaithersburg, MD. Our gratitude is extended to the administrative and operating staff stationed at the computer center in Gaithersburg, the ERL headquarters in Boulder, and GFDL in Princeton for logistical support required for this endeavor. In the analysis phase of this study, NCL is particularly indebted to Professor J. M. Wallace for generously sharing his insights on the preliminary results, and for his constant encouragement of this model investigation. The initial draft of this manuscript has been read by A. Broccoli, I. Held, Y. Kushnir and A. Oort, whose comments have led to substantial improvement of this work. The detailed and constructive remarks of an anonymous official reviewer were particularly helpful in clarifying some of the implications of the model results. The figures in this paper have been drafted by the Scientific Illustration Group at GFDL.

REFERENCES

Alexander, R. C., and R. L. Mobley, 1976: Monthly average sea-surface temperature and ice-pack limits in a 1° global grid. *Mon. Wea. Rev.*, **104,** 143–148.

Barnston, A., and R. E. Livezey, 1987: Classification, seasonality and persistence of low-frequency circulation patterns. *Mon. Wea. Rev.*, **115,** 1083–1126.

Bjerknes, J., 1966: A possible response of the atmospheric Hadley circulation to equatorial anomalies of ocean temperature. *Tellus,* **18,** 820–829.

——, 1969: Atmospheric teleconnections from the equatorial Pacific. *Mon. Wea. Rev.*, **97,** 163–172.

Blackmon, M. L., 1976: A climatological spectral study of the 500 mb geopotential height in the Northern Hemisphere. *J. Atmos. Sci.*, **33,** 1607–1623.

——, J. M. Wallace, N.-C. Lau and S. L. Mullen, 1977: An observational study of the Northern Hemisphere wintertime circulation. *J. Atmos. Sci.*, **34,** 1040–1053.

——, J. E. Geisler and E. J. Pitcher, 1983: A general circulation model study of January climate anomaly patterns associated with interannual variation of equatorial Pacific sea surface temperatures. *J. Atmos. Sci.*, **40,** 1410–1425.

——, Y.-H. Lee and J. M. Wallace, 1984: Horizontal structure of 500 mb height fluctuations with long, intermediate and short time scales. *J. Atmos. Sci.*, **41,** 961–979.

Boer, G. J., 1985: Modelling the atmospheric response to the 1982/83 El Niño. *Coupled Ocean Atmosphere Models,* Elsevier Oceanography Ser., Vol. 40, J. C. J. Nihoul, Ed., 7–17.

Bunker, A. F., 1976: Computations of surface energy flux and annual air–sea interaction cycles of the North Atlantic Ocean. *Mon. Wea. Rev.*, **104,** 1122–1140.

Chen, W. Y., 1982: Fluctuations in Northern Hemisphere 700 mb height field associated with the Southern Oscillation. *Mon. Wea. Rev.*, **110,** 808–823.

Davis, R. E., 1976: Predictability of sea surface temperature and sea level pressure anomalies over the North Pacific Ocean. *J. Phys. Oceanogr.*, **6,** 249–266.

Esbensen, S. K., 1984: A comparison of intermonthly and interannual teleconnections in the 700 mb geopotential height field during the Northern Hemisphere winter. *Mon. Wea. Rev.*, **112,** 2016–2032.

Frankignoul, C., 1985: Sea surface temperature anomalies, planetary waves, and air-sea feedback in the middle latitudes. *Rev. Geophys.*, **23,** 357–390.

——, and A. Molin, 1988: Response of the GISS general circulation model to midlatitude sea surface temperature anomaly in the North Pacific. *J. Atmos. Sci.*, **45,** 95–108.

Held, I. M., and I-S. Kang, 1987: Baratropic models of the extratropical response to El Niño. *J. Atmos. Sci.*, **44,** 3576–3586.

Horel, J. D., 1981: A rotated principal component analysis of the interannual variability of the Northern Hemisphere 500 mb height field. *Mon. Wea. Rev.*, **109,** 2080–2092.

——, and J. M. Wallace, 1981: Planetary scale atmospheric phenomena associated with the Southern Oscillation. *Mon. Wea. Rev.*, **109,** 813–829.

Hoskins, B. J., and D. J. Karoly, 1981: The steady linear response of a spherical atmosphere to thermal and orographic forcing. *J. Atmos. Sci.*, **38,** 1179–1196.

Kang, I.-S., and N.-C. Lau, 1986: Principal modes of atmospheric variability in model atmospheres with and without anomalous sea surface temperature forcing in the tropical Pacific. *J. Atmos. Sci.*, **43,** 2719–2735.

Keshavamurty, R. N., 1982: Response of the atmosphere to sea surface temperature anomalies over the equatorial Pacific and the teleconnections of the Southern Oscillation. *J. Atmos. Sci.*, **39,** 1241–1259.

Kutzbach, J. E., R. M. Chervin and D. D. Houghton, 1977: Response of the NCAR general circulation model to prescribed changes in ocean surface temperature. Part I: Mid-latitude changes. *J. Atmos. Sci.*, **34,** 1200–1213.

Lanzante, J. R., 1984: A rotated eigenanalysis of the correlation between 700 mb heights and sea surface temperatures in the Pacific and Atlantic. *Mon. Wea. Rev.*, **112,** 2270–2280.

Lau, N.-C., 1978: On the three-dimensional structure of the observed transient eddy statistics of the Northern Hemisphere wintertime circulation. *J. Atmos. Sci.*, **35,** 1900–1923.

——, 1981: A diagnostic study of recurrent meteorological anomalies appearing in a 15-year simulation with a GFDL general circulation model. *Mon. Wea. Rev.*, **109,** 2287–2311.

——, 1985: Modeling the seasonal dependence of the atmospheric response to observed El Niños in 1962–76. *Mon. Wea. Rev.*, **113,** 1970–1996.

——, 1988: Variability of the observed midlatitude storm tracks in relation to low-frequency changes in the circulation pattern. *J. Atmos. Sci.*, **45,** 2718–2743.

——, and E. O. Holopainen, 1984: Transient eddy forcing of the time-mean flow as identified by geopotential tendencies. *J. Atmos. Sci.*, **41,** 313–328.

——, and M. J. Nath, 1987: Frequency dependence of the structure and temporal development of wintertime tropospheric fluctuations—Comparison of a GCM simulation with observations. *Mon. Wea. Rev.*, **115,** 251–271.

——, and A. H. Oort, 1985: Response of a GFDL general circulation model to SST fluctuations observed in the tropical Pacific Ocean during the period 1962–1976. *Coupled Ocean Atmosphere Models,* Elsevier Oceanography Ser., Vol. 40, J. C. J. Nihoul, Ed., 289–302.

Lough, J. M., 1986: Tropical Atlantic sea surface temperatures and rainfall variations in Subsaharan Africa. *Mon. Wea. Rev.*, **114**, 561–570.

Manabe, S., and D. G. Hahn, 1981: Simulation of atmospheric variability. *Mon. Wea. Rev.*, **109**, 2260–2286.

——, and J. L. Holloway, Jr., 1975: The seasonal variation of the hydrologic cycle as simulated by a global model of the atmosphere. *J. Geophys. Res.*, **80**, 1617–1649.

Nakamura, H., M. Tanaka and J. M. Wallace, 1987: Horizontal structure and energetics of Northern Hemisphere wintertime teleconnection patterns. *J. Atmos. Sci.*, **44**, 3377–3391.

Namias, J., 1969: Seasonal interactions between the North Pacific Ocean and the atmosphere during the 1960's. *Mon. Wea. Rev.*, **97**, 173–192.

——, and D. R. Cayan, 1981: Large-scale air–sea interactions and short-period climatic fluctuations. *Science*, **214**, 869–876.

——, X. Yuan and D. R. Cayan, 1988: Persistence of North Pacific sea surface temperature and atmospheric flow patterns. *J. Climate*, **1**, 682–703.

Palmer, T. N., and D. A. Mansfield, 1984: Response of two atmospheric general circulation models to sea-surface temperature anomalies in the tropical east and west Pacific. *Nature*, **310**, 483–485.

——, and Z.-B. Sun, 1985: A modelling and observational study of the relationship between sea surface temperature in the northwest Atlantic and the atmospheric general circulation. *Quart. J. Roy. Meteor. Soc.*, **111**, 947–975.

Panofsky, H. A., and G. W. Brier, 1958: *Some Applications of Statistics to Meteorology*. The Pennsylvania State University, 224 pp.

Pitcher, E. J., M. L. Blackmon, G. T. Bates and S. Muñoz, 1988: The effect of North Pacific sea surface temperature anomalies on the January climate of a general circulation model. *J. Atmos. Sci.*, **45**, 173–188.

Ratcliffe, R. A. S., and R. Murray, 1970: New lag associations between North Atlantic sea temperature and European pressure applied to long-range weather forecasting. *Quart. J. Roy. Meteor. Soc.*, **96**, 226–246.

Reynolds, R. W., 1983: A comparison of sea surface temperature climatologies. *J. Climate. Appl. Meteor.*, **22**, 447–459.

Richman, M. B., 1986: Rotation of principal components. *J. Climatol.*, **6**, 293–335.

Rowntree, P. R., 1972: The influence of tropical east Pacific ocean temperatures on the atmosphere. *Quart. J. Roy. Meteor. Soc.*, **98**, 290–321.

——, 1976: Response of the atmosphere to a tropical Atlantic ocean temperature anomaly. *Quart. J. Roy. Meteor. Soc.*, **102**, 607–625.

Shukla, J., and B. Bangaru, 1979: Effect of a Pacific sea-surface temperature anomaly on the circulation over North America: A numerical experiment with the GLAS model. *Report of the JOC Study Conference on Climate Models: Performance, Intercomparison and Sensitivity Studies*, Vol. 1, WMO, 501–518.

——, and J. M. Wallace, 1983: Numerical simulation of the atmospheric response to equatorial Pacific sea surface temperature anomalies. *J. Atmos. Sci.*, **40**, 1613–1630.

Simmons, A. J., 1982: The forcing of stationary wave motion by tropical diabatic heating. *Quart. J. Roy. Meteor. Soc.*, **108**, 503–534.

Tokioka, T., A. Kitoh and A. Katayama, 1986: Atmospheric response to the sea surface temperature anomalies in the mature phase of El Niño: Numerical experiment under the perpetual January conditions. *J. Meteorol. Soc. Jpn.*, **64**, 347–362.

van Loon, H., and J. C. Rogers, 1981: The Southern Oscillation. Part II: Associations with changes in the middle troposphere in northern winter. *Mon. Wea. Rev.*, **109**, 1163–1168.

von Storch, H., and H. A. Kruse, 1985: The extra-tropical atmospheric response to El Niño events—a multivariate significance analysis. *Tellus*, **37A**, 361–377.

Wallace, J. M., and D. S. Gutzler, 1981: Teleconnections in the geopotential height field during the Northern Hemisphere winter. *Mon. Wea. Rev.*, **109**, 784–812.

——, and Q.-R. Jiang, 1987: On the observed structure of the interannual variability of the atmosphere/ocean climate system. *Atmospheric and Oceanic Variability*. Roy. Meteor. Soc., H. Cattle, Ed., 17–43.

——, C. Smith and Q.-R. Jiang, 1990: Spatial patterns of atmosphere/ocean interaction in the northern winter. *J. Climate*, **3**, 990–998.

Walsh, J. E., and M. B. Richman, 1981: Seasonality in the associations between surface temperatures over the United States and the North Pacific Ocean. *Mon. Wea. Rev.*, **109**, 767–783.

Weare, B. C., 1977: Empirical orthogonal function analysis of Atlantic ocean surface temperature. *Quart. J. Roy. Meteor. Soc.*, **103**, 467–478.

——, A. Navato and R. E. Newell, 1976: Empirical orthogonal analysis of Pacific Ocean sea surface temperatures. *J. Phys. Oceanogr.*, **6**, 671–678.

Woodruff, S. D., R. J. Slutz, R. L. Jenne and P. M. Steurer, 1987: A comprehensive ocean-atmosphere data set. *Bull. Amer. Meteor. Soc.*, **68**, 1239–1250.